



# A Roadmap for Obtaining and Implementing Heat Flux Measurements in the Hypersonic Environment

Nicholas Tiliakos<sup>1</sup>, Jeff DeSorbo<sup>2</sup>, Nick Martin<sup>3</sup>  
*Innoveering, LLC, Ronkonkoma, NY, 11779, USA*

Valerio Viti<sup>4</sup>  
*ANSYS Inc., Lebanon, NH, 03766, USA*

Stuart Laurence<sup>5</sup> and Oded Rabin<sup>6</sup>  
*University of Maryland, College Park, MD, 20742, USA*

Dealing with the large aerodynamic heating loads encountered during sustained hypersonic flight is one of several key problems facing hypersonic vehicle designers. There remains a critical need for high-quality validation data from experiments and for accurate heat flux measurements from heat flux sensors integrated into the hypersonic vehicle. Measurement of heat flux on a hypersonic test article (ground or flight) poses many challenges, from determining the best location for the measurements, ensuring survivability, reliability to test article integration with minimal disturbance to the vehicle's TPS and to the sensor's performance. An overview of the numerous challenges of measuring heat flux to a hypersonic vehicle/test article is described and a simple "roadmap", with lessons learned, is presented for implementing these sensors in the hypersonic environment. An overview of some calibration techniques for heat flux sensors is presented, with a focus on shock tube analysis, design. A combination of 3D transient CFD/thermal-structural ANSYS analysis is presented, showing thermal-structural results of a miniature fast response heat flux sensor, integrated into a test article. The analysis shows how matching and mismatching of test article material versus sensor material affects the sensor's thermal-structural response as well as how best to ensure it survives the hypersonic environment.

## I. Nomenclature

CCC	=	Carbon Carbon Composites
$C_p$	=	Specific heat capacity, [J/kg K]
d	=	Shock tube inner diameter, [in]
E	=	Young's Modulus, [Pa]
h	=	Heat transfer coefficient, [W/m K]
HTTE	=	High Temperature Thermoelectrics
$l_{DR}$	=	Shock tube driver length, [ft]
$l_{DN}$	=	Shock tube driven section length, [ft]
OML	=	Outer Mold Line
P	=	Pressure, [Pa or psia]
S&T	=	Science & Technology
T	=	Gas Temperature, [K]

<sup>1</sup> Chief Technologist/Principal, AIAA Senior Member

<sup>2</sup> Mechanical Engineer, AIAA Member

<sup>3</sup> Project Engineer, AIAA Member

<sup>4</sup> Aerospace and Defense Lead, AIAA Senior Member

<sup>5</sup> Associate Professor, Aerospace Engineering, AIAA Senior Member

<sup>6</sup> Associate Professor, Materials Science and Engineering

t	=	Test time, [msec or sec]
T&E	=	Testing & Evaluation
TPS	=	Thermal Protection System
$\Delta T$	=	Temperature difference/gradient, [K]
UHT	=	Ultra-High Temperature

#### Subscripts

e	=	post reflected shock region @ thermal boundary layer edge;
w	=	shock tube driven section end wall

#### Greek Symbols

$\alpha$	=	thermal diffusivity, [m <sup>2</sup> /sec]
$\theta_w$	=	$T_w/T_e$
$\kappa$	=	Thermal conductivity, [W/m K]
$\varepsilon$	=	Emissivity

## II. Introduction/Background

With the rise of the Pacific Rim economies, as well as the shifting global military tactics and strategies, it has become clear that a hypersonic transport or missile is of relevance to the United States Armed Forces. To this end, the U.S. has recently been increasing its R&D activities in hypersonic technology, both ground and flight test articles, for both commercial and military purposes. Hypersonic flight poses many challenges, from aerodynamics, propulsion, high temperature materials, aero-thermochemistry, thermal management, stability and control and reliability. Research and development activities are being conducted on new classes of hypersonic vehicles that will need to sustain a Mach 3 to Mach 6+ flight, en route to their mission destination. Due to the stringent, competing requirements of low weight structures in the harsh high temperature environment of hypersonics, new materials, particularly ultra-high temperature (UHT) carbides and borides, will be pushed to their limits. To determine how these new materials function in the hypersonic environment they will need to be extensively tested and evaluated on the ground via sensor diagnostics, and eventually in flight, subject to realistic aerothermal test conditions, including real gas/non-equilibrium effects, convective/radiative heating, dissociation/ionization i.e. material-plasma interactions, viscous-shock interactions, boundary layer transitions and surface catalysis, with highly coupled physics, affecting the material's interaction/response to this harsh environment.

Hypersonic vehicles experience very high aero-thermodynamic heating and structural loads encountered during sustained flight. Surviving these high thermal and mechanical loads requires proper thermal management, cooling, TPS (Thermal Protection System) design and material selection. TPS design requires knowledge of thermal loads, i.e. heat flux, total heat transfer, duration, wall temperature distribution. These loads are passed onto the thermal-structural analyst and the structural engineer, who select the proper TPS material, determine the TPS design, thickness, reinforcement, that minimizes weight and ensures vehicle survivability for the duration of the test/mission. While computational fluid dynamics simulations are constantly improving in their ability to accurately predict aerothermal loading, there remains a critical need for high-quality *experimental validation data*, eg. surface temperature, pressure, shear stress and heat flux, that not only validates the TPS/thermal management design but also helps to anchor the models and analysis used to predict the aero-thermodynamic conditions.

There is therefore a need in the hypersonic test and evaluation/science and technology (T&E/S&T) community for the development of accurate sensors to evaluate the hypersonic vehicle's material response, aerodynamic and propulsive behavior in this environment as well as to evaluate the aero-thermodynamic loads, i.e. heat flux, surface temperature. At high Mach numbers, non-equilibrium and real gas effects, including dissociated/ionized species, variable specific heat ( $\gamma \neq 1.4$ ), compressibility effects, laminar to turbulent transition, also affect the surrounding fluid's thermal properties and transport properties, within the boundary layer, which in turn significantly influence the heat transfer to the material, as well as the shock angles, boundary layer transitions and instabilities. These are highly coupled phenomena, coupling into the aerodynamic, thermal-structural loading, oxidation and ablation phenomena of the material protecting the hypersonic vehicle. Simulating these conditions on the ground, allowing for design-test/evaluation and re-design activities, prior to flight, is an invaluable part of a methodical and thorough engineering process, especially needed for hypersonic vehicle development.

It is important to accurately measure heat flux in a hypersonic environment, since knowledge the heat flux into the vehicle helps designers to accurately design the appropriate amount of TPS and/or thermal management for the vehicle. Most often, due to uncertainties in the thermodynamic state of the air surrounding the vehicle, engineers will over design the TPS thickness, or the amount of coolant required, thus contributing to increased vehicle structural and fuel weight, leading to a reduced payload mass fraction. The ability to accurately measure heat flux will assist in anchoring/validating thermal load models as well as assisting in determining boundary layer transition from laminar to turbulent, all of which are required for vehicle TPS design.

It is our intent for this work to provide the authors' view point on lessons learned and a basic roadmap for implementing heat flux measurements in the hypersonic environment. Our hope is to assist new test engineers/instrumentation engineers entering the hypersonic T&E/S&T community, with the understanding that this is not a "one size fits all" recipe, but one that is very much dependent on the application.

### III. The Hypersonic Environment

Due to the very harsh environment of hypersonics, the engineer is left with many challenges to address in everything from the design of the vehicle's TPS/thermal management system, to the propulsion, aerothermodynamics, stability and control to name a few. The hypersonic flow field poses additional complexities with regards to the thermal-mechanical non-equilibrium environment, compressibility effects for  $M \geq 3$  and for conditions above Mach 15, where air dissociation and weak ionization occur, as discussed below. Under these conditions, there can also be complex wall-surface/gas interactions, shock-boundary layer and shock-shock interactions, which affect the heat flux rate into the hypersonic vehicle, potentially amplifying it beyond initial design point. Some of these surface-flowfield interactions include surface catalysis and surface radiation emittance, both functions of surface temperature, strongly coupled to the surface-flowfield interaction, affecting the boundary layer conditions and heat transfer to the vehicle.

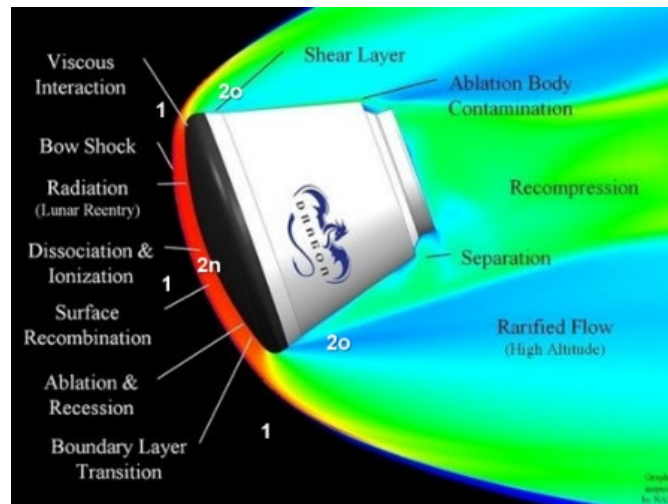


Fig.1 A typical hypersonic environment.

The hypersonic environment is extremely challenging, both to predict, to design for and to replicate aspects accurately in a ground test facility. This is because the flow regimes, from supersonic ( $1 \leq M \leq 4.9$ ) to hypersonic,  $M \geq 5$ , differ significantly, from aerodynamics, thermal-fluid, boundary layer-shock interactions, non-equilibrium and real gas effects, heat transfer, to name a few. Besides the thermal/momentum boundary layers, there is an entropy layer that drives the vorticity downstream of the shock, making it difficult to predict/model boundary layer properties/physics. The entropy layer, Fig. 1, interacts with the viscous boundary layer, producing complicated aerothermodynamic flow. Viscous effects within the boundary layer, "the viscous-inviscid interaction", leads to an increase in temperature within the layer, a decrease in density and increase in boundary layer thickness which in turn affects the surface pressure, heat flux, skin friction to the vehicle. There are coupled interactions between the viscous boundary layer, the thin shock layer and outer inviscid flow stream affecting the vehicle's surface and therefore its material response, aerodynamics, stability, thermal-structural characteristics. Adding to the complexity, all these effects can be highly coupled, with varying thermal, fluid and transport properties. The environment that hypersonic test engineers, materials engineers and designers are trying to understand is depicted in Figure 2, [3].

Addressing these challenges requires a combination of thorough ground (and flight testing) along with advanced analysis/computational modeling. Both experiments/testing and modeling are required. However models require validation/anchoring and as such advanced sensors and diagnostics for measuring thermodynamic properties within the vehicle's boundary layer, at and within the vehicle's structure and determination of thermal and mechanical loads on the vehicle are needed. One such critical measurement is heat flux into the vehicle, which will help the engineer design the vehicle's TPS such that it falls within the allowable structural safety factors and is not overdesigned, leading to increase in structural mass fraction at the expense of increasing payload fraction.

#### IV. Current State of the Art Heat Flux Sensors for Hypersonic Applications

Much attention has focused on the development of heat-flux sensors and data-reduction methodologies for short-duration hypersonic facilities [1]. Traditional sensors, such as fast-response coaxial thermocouples and thin-film gauges, measure the surface temperature time history. The heat flux can then only be derived from the temperature history under a number of assumptions, including heat transfer into a semi-infinite body. Thermocouples are survivable under even harsh flow conditions but have relatively low sensitivities, limiting the accuracy of the derived heat flux. Thin-film gauges, on the other hand, are highly sensitive but fragile, limiting their usefulness in facilities in which a high level of particulates is present in the free-stream flow. Regardless, the assumptions traditionally used for deriving the heat flux from the temperature history for both these sensor types may become invalid in the longer test durations typical of blowdown facilities.

**Table 1 Brief Summary of CSOTA Heat Flux Sensors [1, 2]**

Heat Flux Sensor Type	Construction	Description/Use of Technique	Pros	Cons
<b>Coaxial Thermocouple Gages</b>	2 Coaxial TCs: 1st T/C is embedded into surface of cylindrical sensor body. Inside is 2nd T/C, concentric to 1st, with insulation separation. These can be swaged into cylin packaging; @ one end is junction + metallic plating. TCs are coated with 0.0005" thk ceramic insulation of high dielectric strength. TC junction formed by vacuum depositing metallic coating to form bond of 1-2 micron thk. Heat flux is indirectly determined from temperature signal, based on 1D heat conduction into semi-infinite body (same as for the thin film gage).	1-measures Tsurf directly, calculate heat flux; 2-flush mounted to structure; 3-micro-second response time to metal wall Tsurf changes; 4-very small form factor, ~O(mms); 5-precise location of TC	1-robust, survive harsh conditions; 2-small form factor; 3-robust, durable, withstands high P and qdot 4-accurate position of TC junction allows precise Tsurf loc measmt; 5-microsecond response time 6-small form factor/conforms to curved surface well.	1-indirect measmt of qdot through analytic heat transfer eqn (assumes semi-infinite body) reliant on surface temp time's history measurement. 2-the deduced heat flux is in direction perpendicular to measuring surface
<b>Thin Film Gages</b>	Consists of ceramic substrate (zirconium oxide), with sputtered thin Ni or Pt film. Two Pt wires embedded into the substrate, with constant current (7-10 mA) supplied. Voltage change across the thin film is directly measured & related to substrate surface temperature. It's assumed that the substrate thin film has no influence on its surface temperature. Heat flux is indirectly determined from temperature signal, based on 1D heat conduction into semi-infinite body (same as for the coaxial thermocouple gage).	1-measures Tsurf directly, calculate heat flux; 2-flush mounted to structure; 3-micro-second response time	1-provide better signal levels than CTGs; 2-more sensitive than TCs;very high sensitivity; 3-microsecond response time	1-Less robust than CTGs (since the sputtered thin metallic film may be destroyed by particle impact or high thermal stress delaminating the thin film). 2-Have to be individually calibrated; (temperature sensitive therefore needs temp compensation for Tsurf>50 degC 3-rely on surface T dependent thermal properties; 4-better for low heat flux, clean environments NOT high heat flux harsh environment w/particle impacts; 5-not ideal for continuous flow tunnels due to film survivability problems.
<b>Gardon Gage</b>	1-circular-foil gage used primarily for measuring high heat flux; 2-foil connected to sensor body & to a thin wire at the center, these form the hot- and cold joint of a thermocouple. 3-Direct heat flux generates a signal; 4-It is typically water-cooled; 5-does not require any power to operate; 6-thermocouple sensor is covered w/black coating to enhance heat absorption..has flat spectrum 300-50,000 nm, cosine response	1-thermocouple junction between thin foil and sensor body/thin circular disk, forms thermocouple junction;	1-simple construction; 2-direct measurement of extremely high heat flux; 3-does not require power;	1-water cooled
<b>Schmidt-Boelter Gage</b>	Similar to Gardon gage, but with a plated constantan wire wrapped around an insulating chip.	1-application in continuous flow wind tunnels & flight tests;	1-excellent durability; 2-good sensitivity; 3-output directly proportional to direct heat flux; 4-max service temperature ~370 °C	1-calibration can be challenging, especially @ elevated temperatures to account for sensor material property variations with temperature; 2-range is more limited compared to Gardon gage.

**Table 1 Brief Summary of CSOTA Heat Flux Sensors (Continued) [1, 2]**

Heat Flux Sensor Type	Construction	Description/Use of Technique	Pros	Cons
Heat Flux (via Thermocouples)	1-array of individual thermocouples, strategically placed @ known distances to indirectly measure heat flux via Fourier's Law.	Can be used to back out heat flux. Frequency response depends on the mass of the active junction. Can be brought down to a few microseconds. Thermocouples surface mounted in the test model give the temperature at set points on the model. These temperatures can be used to back out heat flux, and allow for the detection of laminar to turbulent transition.	1-simple construction; 2-use readily available, off-the-shelf components	1-indirect measurement that relies on accurate knowledge of TC location; 2-relies on assumption of 1D heat transfer to apply 1D Fourier Heat eqn.
Heat Flux (IR Camera)	1-optical pyrometer or infrared pyrometer	IR camera is used to acquire surface temperature on large portions of test model. Data can then be post processed to calculate heat flux and locate the transition onset location. Provides quantitative measures of heat transfer. These can be used to detect transition locations.	1-provides continuous acquisition	1-limited to applications with optical access; 2-expensive; 3-requires some knowledge of object's emissivity characteristics @ elevated temperatures
Atomic Layer Thermopile (ALTP)	leverages high temperature thermoelectric material and the Transverse Seebeck effect	Fast-response heat-flux gauge with a spectral resolution near 1 MHz. Based on the transverse Seebeck effect. Output signal is directly proportional to heat-flux density.	1-measures direct heat flux; 2-small form factor; 3-fast response (micro-sec)	1-Commercially available ALTP sensors are limited to relatively low temperatures, low heat flux; 2-Commercially available ALTP sensors have large form factor and low upper temperature limit
Thermal/Pressure Sensitive Paints	1-Thermosensitive paints result in color changes proportional to level of heat flux;	Specific paints react when exposed to pressure/temperature. Pictures taken at specific points during the test allow for the location of regions of different pressure/temperature.	1-non-intrusive; 2-high spatial resolution; 3-relatively inexpensive	1-typically requires re-application of paint; 2-limited to applications with optical access

A relatively recent development for heat-flux measurements in hypersonic flows is the atomic layer thermopile (ALTP) sensor. Making use of the transverse Seebeck effect in an obliquely layered YBCO thin film, the ALTP produces an output voltage that is directly proportional to the incident heat flux, an immediate advantage over traditional sensors. Moreover, ALTP sensors exhibit a usable frequency range up to several hundred kilohertz (-3dB at 300 kHz) allowing them to be employed even for high-frequency boundary-layer instability measurements [34]. The main disadvantage of the ALTP sensor is the large surface footprint of the sensor housing (approximately 8 mm diameter), making it impossible to incorporate into complex model geometries – especially leading edges with small radii of curvature – and limiting sensor density. A further limitation is a maximum quoted operating temperature of 50° C [33], though measurements at conditions for which the surface temperature would have substantially exceeded this value can be found in the literature [35]. A brief summary of CSOTA heat flux sensors is presented in Table 1.

## V. Challenges & Lessons Learned: Implementing Heat Flux Sensors for Hypersonic Applications

There are numerous challenges with designing and implementing instrumentation within structures exposed to the hypersonic environment, some of which are outlined in this section, that apply in a general sense to harsh environment sensors, with a subset that are specific to heat flux instrumentation. The hypersonic environment was addressed earlier, here we review some of the challenges in implementing heat flux sensors to interrogate this environment. Reviewing the challenges in implementing and using heat flux sensors is many times specific to the application involved. Keeping this in mind while also attempting to “generalize” the problem into a “universal solution” is not our goal here, nor is it possible, as this problem offers the researcher many unique challenges. However, our purpose here is to provide a succinct overview of the current state of the art in implementing heat flux sensors for hypersonic applications, with a perspective from the authors’ experience in both ground and flight test vehicles. It is important that the instrumentation or test engineer remember that implementing heat flux sensors must consider the materials, test duration and the sensor type. For very short duration, highly transient tests, it may suffice that a thin film gage be used as opposed to a Schmidt-Boelter gage. Below we review some of the challenges of implementing heat flux instrumentation as well as some suggestions/recommendations, to help advance knowledge in this area.

A. *Sensor Compatibility & Integration with Structure*: Compatibility issues related to integration of the sensor within the structure, i.e. will the physical intrusion of the sensor within the structure affect the structure’s material response to its surrounding environment in an adverse manner, different than if the sensor were not installed. This is especially important in actively cooled structures, [2]. Proper implementation of heat flux sensors into the structure should ideally begin with careful consideration of how best to integrate the sensor into the structural by considering material compatibility, i.e. the  $(\rho C_p k)^{1/2}$  of the structure (or “parent” material) should closely match the  $(\rho C_p k)^{1/2}$  of the sensor’s material. The presence of the sensor must not alter the integrity of the structure from its thermal character/response to its mechanical/structural behavior. The sensor should not perturb its surroundings and be as

non-intrusive as possible. Poor integration of the sensor into the structure not only affects the sensor's performance to provide accurate and representative heat flux measurements but it could also adversely affect the structure's nominal behavior from its aerodynamic to its mechanical characteristics [2].

B. *Sensor Location Within Structure:* Measuring heat flux/heat transfer into a structure is a function of multiple, coupled variables including: thermal-mechanical properties ( $E$ ,  $\kappa$ ,  $\alpha$ ,  $C_p$ ,  $T$ ), temperature, pressure, and location. Specifically, heat flux also depends on the following: (i) the conditions ( $P$ ,  $T$ ) within the fluid boundary layer surrounding the sensor; (ii) the boundary layer thickness; (iii) shock-boundary layer and/or shock-shock interactions; (iv) the structure's temperature, its thermal-mechanical properties ( $E$ ,  $\kappa$ ,  $\alpha$ ,  $C_p$ ,  $T$ ); (v) the sensor's temperature, its thermal-mechanical properties ( $E$ ,  $\kappa$ ,  $\alpha$ ,  $C_p$ ,  $T$ ); (vi) is the sensor embedded within the structure. Improper location of the heat flux sensor (or sensors) can lead to poor or inaccurate data, especially if the heat flux is calculated from the temperature gradient via Fourier's law of heat conduction. Accurate knowledge of where the sensor is placed, especially for sensors located within the material during the material's fabrication, where things can shift, etc, is very important to relate the experimental data to the analytical thermal response model.

Proper location of the heat flux sensor should take into account locations where: (i) the flowfield conditions,  $P$ ,  $T$  are known, if possible, so that estimates of temperature gradients  $\Delta T$ , and 'h' (heat transfer coefficient) can provide reasonable approximation of heat transfer; (ii) any shock wave structures can be determined and assessed to see if they affect the heat transfer; (iii) the local thermal-fluid dynamics is relatively simple, without any complex interactions or transitional flows (eg laminar to turbulent flow), such that interpretation of the heat flux/heat transfer data is straightforward and consistent with any assumptions in the data analysis/modeling, eg. view factor considerations, calculations for radiative heat transfer can be complicated in recirculating flows.

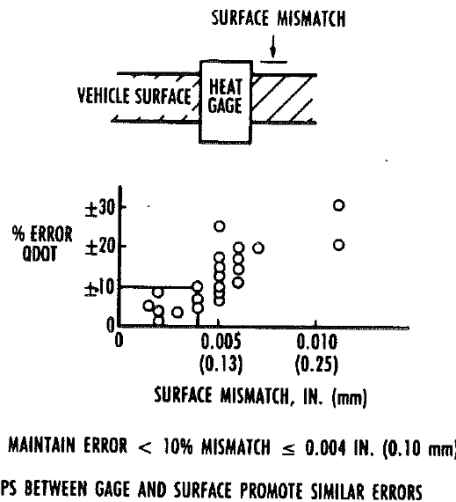


Fig. 2 Effects of heat flux sensor installation mismatch on measurements [1]

C. *Sensor Installation:* If the heat flux sensor is not installed properly into the surface of the test article/vehicle, it could lead to unwanted shock waves, perturbing the boundary layer, affecting the local flowfield aerodynamics and heat transfer. If the sensor is installed such that it protrudes slightly above the vehicle's surface, especially if this perturbation extends beyond the viscous sub-layer, producing a forward facing step, Fig. 2, [1], this could result in a non-trivial leading edge shock emanating from the leading edge of the sensor, adversely affecting the local boundary layer and heat transfer. A mismatch of 0.005" could lead to an error in the sensor's measurement of  $\geq \pm 15\%$  or more, Fig. 2, [1]. Forward facing steps and gaps between the sensor and the structure should be avoided as much as possible. Rearward facing steps, resulting when the sensor is below the vehicle outer mold line (OML) are preferable over forward facing steps, though ideally both should be avoided. Rearward facing steps would result in weak Prandtl-Meyer expansion fans with do not perturb the flow as much as oblique shocks. Such disturbances can best be assessed, prior to sensor installation, via CFD; later in this paper, CFD/thermal FEA results are presented which show that a 0.05 mm recess of a heat flux sensor results in very weak shock waves over the sensor; in this case they do not perturb the local boundary layer or heat transfer, Fig. 15-Fig. 16. In addition to analysis, it may also prove useful to assess such sensor installation miscues during the calibration phase, by performing calibrations

with the heat flux sensor at different installation depths, i.e. flush with test article wall, 0.005” below wall, 0.010” below wall, 0.015” below wall to see how installation error affects heat flux measurement accuracy and output.

Installation of heat flux sensors, or any sensor, into ablative/TPS material, is challenging, not only for the same reasons outlined above, and shown in Figs. 2-3, but also because of the effects, on sensor performance, due to any erosion or recession of the ablative. This is especially concerning for sensors that require direct contact with the environment and are flush mounted to the test article or flight vehicle. Care must be taken when installing heat flux sensors in ablatives, which can recede and expose sensor packaging to the flow, similar to Fig 2, leading to unwanted shock wave disturbances, flow distortion/recirculation in gaps and ultimately distorted heat flux measurements. A potential solution to this challenge is to fabricate the sensor packaging out of the same ablative as the TPS/vehicle skin. Installing sensors into ablatives/composites is briefly discussed below in Section F.

D. *Hot Spots/2D Heat Transfer Effects*: As mentioned earlier, compatibility of the parent material, i.e. test article/vehicle and the sensor’s material is important and should be considered early on in the selection or design of the heat flux sensor. Parent vs sensor material affects sensor’s thermal response, which won’t necessarily be consistent with the parent materials’ wall response, thus affecting the accuracy of the heat flux measurement into the structure. This material mismatch could lead to hot spots and 2D heat transfer affects, each with non-trivial implications. Hot spots are a function of: material mismatch between sensor and parent/test article; test duration; wall temperature distribution; shock-shock/shock-boundary layer interactions; boundary layer laminar to turbulent transition; turbulence and 2<sup>nd</sup> mode instabilities; and thermal stresses leading to material deformations creating gaps, which may lead to increased heat transfer at thermal stress concentrations, i.e. gap heating.

Hot spots will: (i) lead to temperature gradients in multi-directions, i.e. along the surface and through the surface (2D heat transfer), which will make data interpretation challenging since the thermal model may not account for this; (ii) lead to erroneous temperature gradients that result mainly from material mismatch/interaction between the parent and the sensor versus temperature gradients due to the nominal interaction between the sensor and the environment surrounding the parent material/test article; and (iii) potentially causing localized heating which could “bias” the local density, viscosity within the boundary layer, as well as the structure’s wall temperature, thereby affecting the heat transfer between the fluid and the test article. Likewise, 2D heat transfer affects lead to the same consequences as hot spots, but also require more complicated thermal models to interpret the heat flux sensor data, especially if that data is reliant on surface or wall temperature. Hot spots can also lead to erroneous thermal perturbations of the boundary layer.

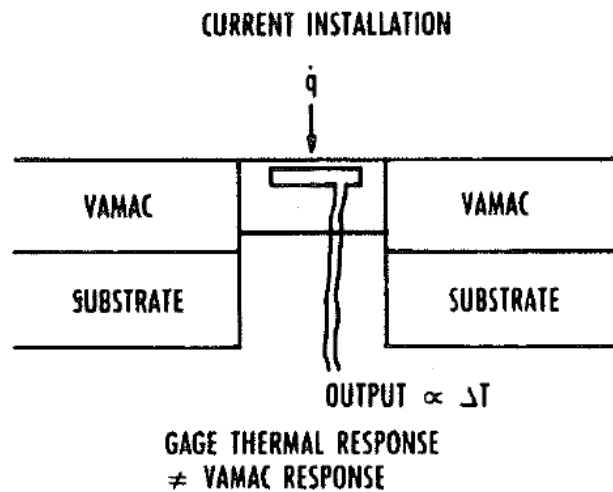


**Fig. 3 Mounting heat flux sensor into parent (i.e. test article) material different from sensor material [1]**

To mitigate the effects of hot spots and 2D heat transfer due to dissimilar materials between the test article (“parent” material) and the heat flux sensor, there are some desirable characteristics of the heat flux sensors: (1) to obtain accurate measurements of highly transient surface temperatures, especially for thin film, coaxial thermocouple gages and ALTP gages (Table 1) it is important that the sensor’s presence have a negligible effect on the temperature

of the test article. To meet such a condition the sensor should not disturb the surface continuity and not bias the heat transfer into the structure.

E. *Non-isothermal Wall Effects*: Non-isothermal wall effects are a result of non-uniform heat distributions, i.e. hot spots, resulting from the same situation, i.e. disparity between the parent and the sensor materials, i.e. the  $(\rho C_p \kappa)^{1/2}$  of the structure (or “parent” material) does not match the  $(\rho C_p \kappa)^{1/2}$  of the sensor’s material. These effects are typically encountered in long duration wind tunnel testing. Uneven temperature distributions are most likely a function of test duration as well, potentially being more pronounced for short duration tests (< several seconds) and becoming less significant as the test duration turns to 10’s seconds to minutes. Like the hot spots, these effects can also lead to erroneous thermal perturbations of the boundary layer. To minimize disturbance to the wall surface temperature, i.e. to mitigate hotspots, the sensor material’s  $(\rho C_p \kappa)^{1/2}$  value should closely match the surface material’s  $(\rho C_p \kappa)^{1/2}$  and the sensor’s form factor should be much smaller than the surface wall thickness.

F. *Sensor Integration Into Advanced Materials/Composites*: Integrating heat flux or any sensors into composites, particularly those suitable for hypersonic applications, eg Carbon Carbon Composites (CCC), is challenging for several reasons: (i) typically the composite is highly anisotropic, resulting in hot spots or 2D heat transfer, unless the sensor material is made of the same material as the parent; (2) need to ensure that the presence of the sensor within the CCC does not adversely affect the structural integrity of the CCC and does not affect the sensor’s performance; and (3) employing fasteners, bolts or threads to secure the sensor in place may prove to be challenging depending on the material thickness; high temperature adhesives could be a viable option to secure sensors within composites. For temperature measurements, it is recommended to follow the ASTM E377 standard. In addition, it is highly recommended to make the sensor packaging out of the same composite as the material it is being embedded into; to make the sensor as small as possible; and to utilize either composite fasteners or high temperature adhesive.

G. *Calibration Challenges*: The main challenge here is ensuring that the calibration approach accurately replicates the heat flux range, temperature range and duration as closely as possible to the final application. Any uncertainties in the calibration should be tracked and incorporated into the final calibration of the heat flux sensor, its performance and its total uncertainty.

Some lessons learned that our team has compiled while working on the design/analysis, fabrication and testing of miniature heat flux sensors are:

1. Care must be taken when using high temperature adhesives, especially for installing heat flux sensors into ablatives/composites. Understanding the behavior, eg. thermal-mechanical properties, of adhesives at high temperatures, consistent with hypersonic applications, is important with regards to bond strength, internal stresses, deformations potential exceeding the material yield strength. Adhesive coating can become brittle and crack at high temperatures, potentially exposing electrical connections and shorting them to the ablative, eg. CCC.
2. ‘1’ above also becomes important if the adhesives require a thinning agent for easier application to the sensor.
3. Testing as often as possible, under relevant conditions, eg. temperature, vibration, etc, is always helpful, though not always possible at conditions. To this end, analysis, whether it be 1D or FEA, is highly recommended to assess sensor thermal-structural response, as presented below in Section VIII.
4. Similar to ‘1’-‘3’ above applies to epoxies, pastes, eg. silver, gold epoxies.
5. Surface roughness of the sensor head/packaging, especially for flush mounted devices, should be minimized as much as possible, since it could affect heat flux measurements, particularly at higher temperatures and Mach numbers.
6. Care is required when incorporating dissimilar materials that make up the heat flux sensor, its electrical connections and packaging. Such connections between dissimilar materials could lead to parasitic thermoelectric effects and/or parasitic capacitance effects (depending on existence of gaps). The authors have experienced issues with use of tin, tinned wire, solder compatibility with certain HTTEs.
7. Sensor cable lengths, connections and cable to data acquisition, should be as short as possible.
8. Wherever possible, position sensor amplifier/electronics circuitry as close to the sensor as possible.
9. When using pulsed lasers to calibrate fast response heat flux sensors fully characterize the laser beam power, intensity, beam width at the sensor’s surface. The sensor’s surface emissivity, absorptivity should be accounted for at relevant wavelengths.

## VI. Suggested Roadmap for Implementing Heat Flux Sensors for Hypersonic Applications

As stated earlier, it is the authors' intention to provide the reader, especially those just entering the hypersonics S&T/T&E community or those involved with test engineering activities of hypersonic engine/vehicle systems, a basic viewpoint on lessons learned (presented in Section V) along with a roadmap for implementing heat flux measurements in the hypersonic environment. This roadmap, Fig. 4, is of course not "all encompassing", as it would surely vary depending on applications, but it is, at a minimum, a listing of methodical activities to be carried out by the instrumentation or test engineer preparing for ground or flight testing of a hypersonic vehicle.

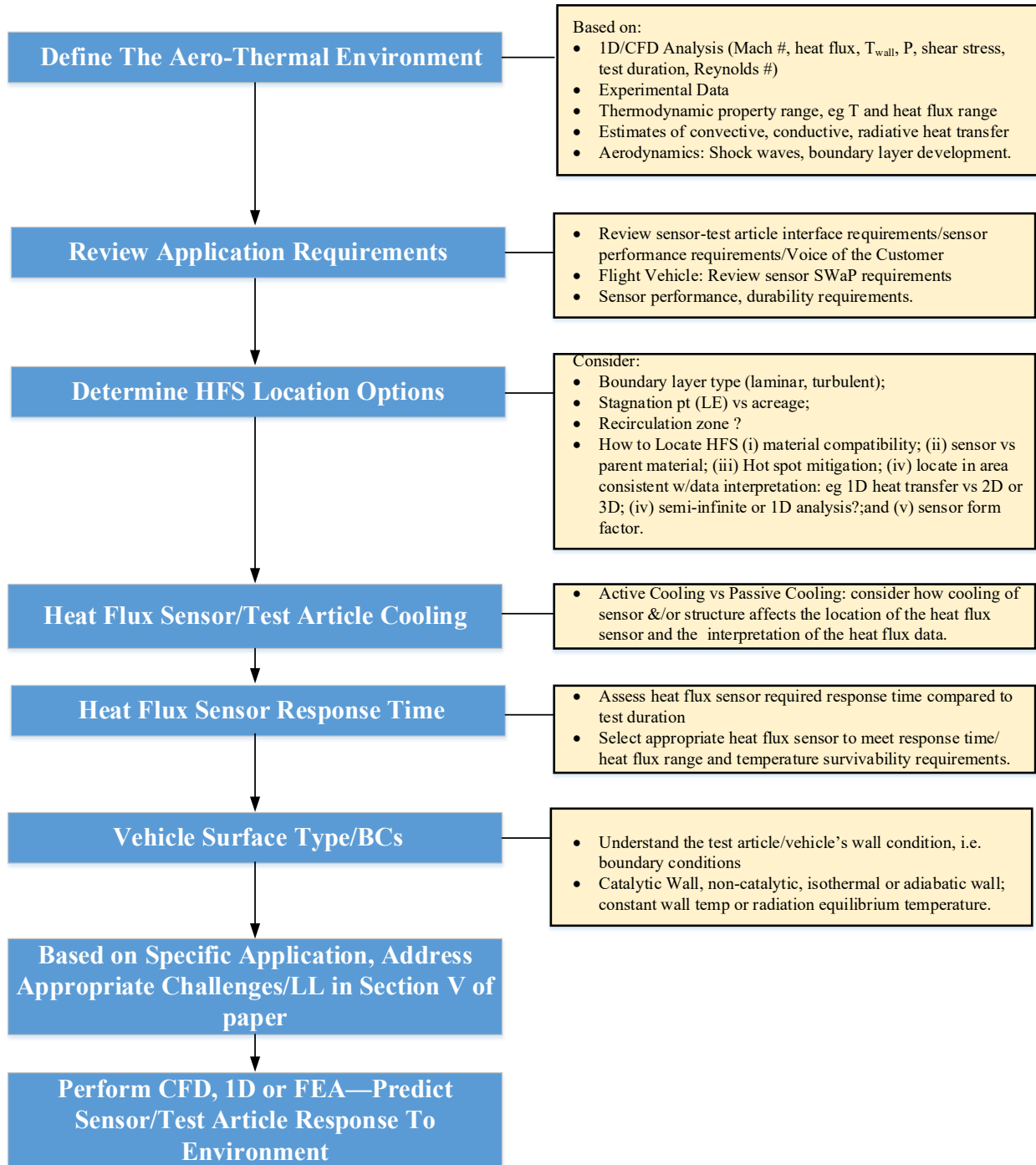


Fig. 4 Overview roadmap for implementing heat flux sensors for hypersonic applications.

## VII. Heat Flux Sensor Calibration

Several methods for calibrating heat flux sensors exist, from heat flux lamps to shock tunnels. Each method has its pros and cons, depending on the sensor response time, temperature and heat flux range desired, accuracy, expected performance/lifetime/durability, budget and schedule. In general, fast response heat flux sensors, on the order of msec or micro-second response time, need to be calibrated dynamically, typically using a pulsed laser with well-defined pulse power and times. Depending on the heat flux sensor, eg thin film or coaxial thermocouple gages, assumptions of “semi-infinite slab” will need to be calibrated over durations that are long enough to satisfy this assumption, also requiring 1D heat conduction. Any assumptions or models used to interpret the heat flux sensor measurements must be satisfied during calibration and ofcourse during the implementation/application. An exhaustive review is not the intention here, rather a brief overview of heat flux sensor calibration techniques, part of our roadmap for implementing these sensors, with references for more detailed research, is presented below.

*NIST Method:* The NIST methodology uses a high temperature blackbody to calibrate heat flux sensors. The blackbody’s heat flux is calculated using an electrically calibrated radiometer. This is a radiative approach to calibrating for heat flux, as presented in Fig. 5. The advantages of this calibration method are that: (i) it is relatively simple and straight forward; (ii) calibrations can be performed over a long period of time; and (iii) NIST traceable. Some of the shortcomings are that it requires a black body with precise temperature control as well as an optical pyrometer/radiometer [3]:

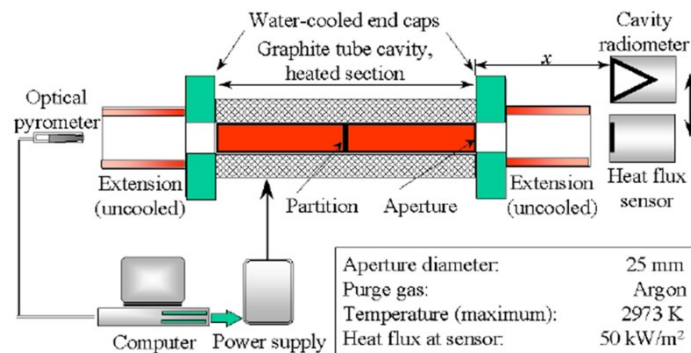


Fig. 5 Schematic of NIST 25 mm variable-temperature blackbody [3]

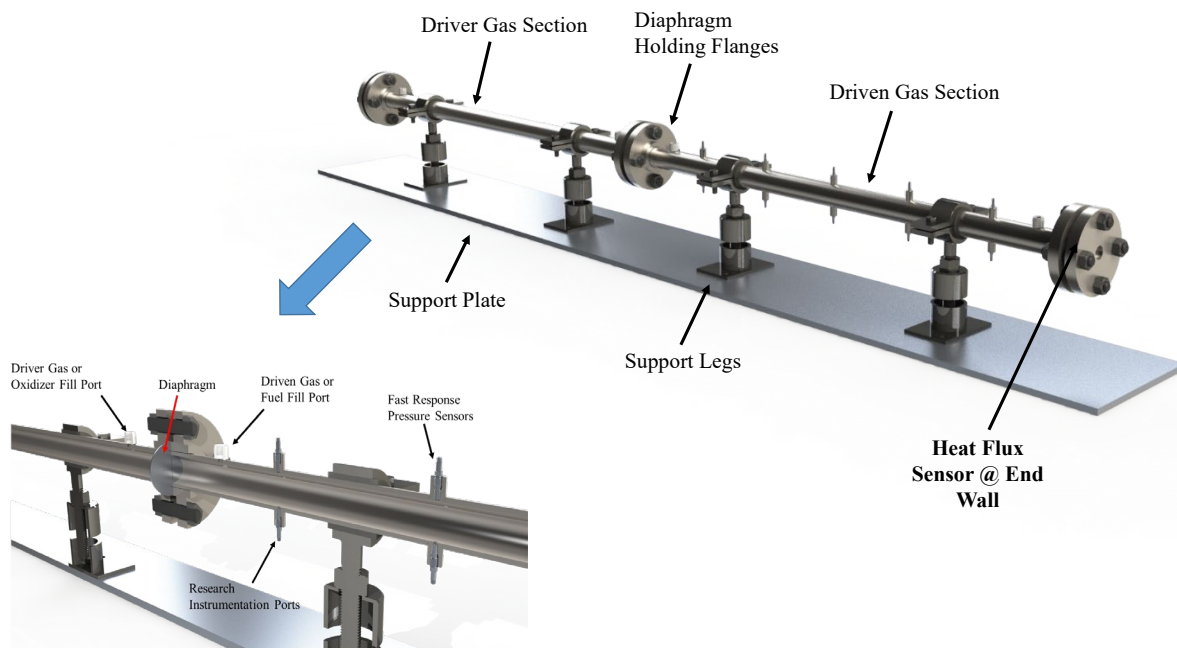
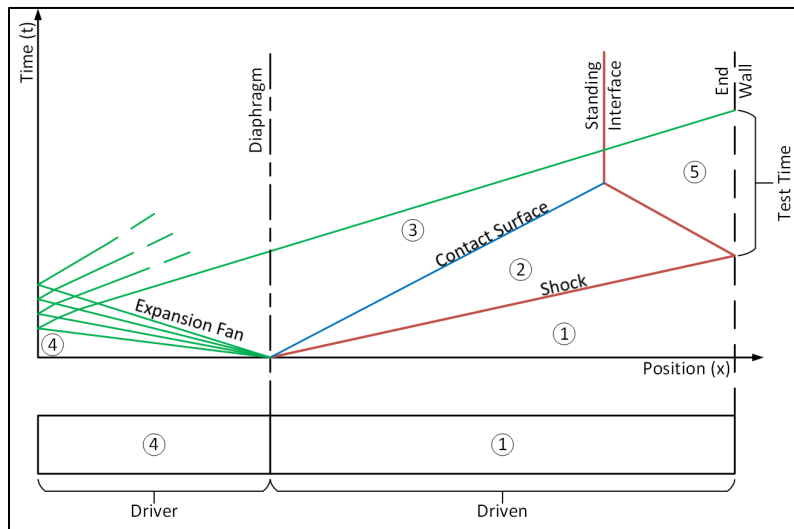


Fig. 6 Schematic of Innoveering’s shock tube facility concept.

**Oil Bath:** In this calibration approach, the sensor is quickly dipped in a reservoir of hot liquid of known temperature and known thermal properties. It must be performed quickly to avoid any fluid motion effects. It appears that this method is used more often to find the thermal coefficient of resistance than to actually calibrate the sensor. The main benefit of this technique is that the method is simple to set up. The disadvantages are that: (i) it relies on the semi-infinite slab assumption; (ii) it is prone to higher uncertainties; and (iii) the heat fluxes generated with this calibration are lower than those achieved in actual test facilities.

**Heat Lamp:** A heat lamp with a known (calibrated) heat flux output at a certain distance is used to calibrate the heat flux sensor. This method could be implemented in two ways: using a factory calibrated a lamp; or purchasing a lamp and calibrating it via a commercially available, calibrated heat flux sensor. Some of the advantages of this method are: (i) simplicity and inexpensive to use; (ii) method allows for the calibration at multiple heat fluxes as long as the lamp power can be tuned. The disadvantages are that the heat fluxes may be lower than those experienced during testing and locating pre-calibrated heat flux lamps can be challenging.

**Shock Tube Method:** Shock tubes, properly designed, provide a very useful calibration tool for heat flux sensors, ensuring a repeatable, fairly constant heat flux (calculated analytically, shown below), over a well-defined, tailored, short time frame (micro-seconds to milli-seconds).



**Fig. 7 Ideal shock tube operation presented in t-x diagram.**

The main idea here is to use a shock tube to generate the necessary heat flux to calibrate the heat flux sensors, place in the end wall of the shock tube. The shock strength can be varied to achieve different heat fluxes, with the driver and driven sections pressurized to desired pressures. A diaphragm separates the driven from the driver section, Fig. 6, with the heat flux sensor, to be calibrated, located at the end wall. The diaphragm is burst, sending a shock wave through the driven section; this shock pressurizes and heats the air in the driven section. This heating can be characterized using known equations, which also provide the heat flux that the sensors are exposed to. The conditions remain constant until the next wave reaches the wall where the sensors are installed. The analysis required to design the appropriate driver, driven pressures that will allow the engineer to tailor the required heat flux profiles over the required time period, is described below. The advantages of using a shock tube are: (i) it allows for simultaneous response time characterization and heat flux calibration; (ii) allows for repeatable, well defined and well characterized heat flux to be delivered to the sensors for calibration; and (iii) different, pre-calibrated, commercially available and off-the-shelf heat flux sensors could be installed into shock tube to verify results. The disadvantages are: (i) requires the design and building of a shock tube; (ii) shock tube calibration tests would need to be run carefully; and (iii) facility may take up a lot of laboratory space. This section will present the engineer with a methodical approach in shock tube analysis, design and implementation for heat flux sensor calibration.

**Shock Tube Analysis:** Calibration of a heat flux sensor in a shock tube was tested experimentally by Marineau and Hornung [3] in the T5 shock tunnel facility. A shock tube may be used to calibrate a heat flux sensor by generating high, test condition relevant heat fluxes in the post-reflected shock region, shown below in Fig. 7 as region 5. The

ideal operation and post-shock conditions of a shock tube can be solved for analytically, and is readily available in existing literature, [4].

Test time within the shock tube begins at the reflection of the unsteady shock, and is ideally ended by the arrival of the reflected expansion fan head. By tailoring the shock tube conditions, a quasi-steady test condition can be maintained at millisecond timescales, with exact test times driven by facility size. The heat flux at the end wall is characterized by neglecting ionization of the gas, allowing the solution for the thermal boundary layer obtained by Fay and Kemp [5] to be reduced to a single ODE. This ODE was integrated by Marineau and Hornung [3] using a shooting method, yielding Eqn. 1.

$$q_w = 1.13 \left[ \frac{\rho_e k_{Ae} c_{pe}}{2t} \right]^{\frac{1}{2}} T_e \left[ \frac{1 - \theta_w^v}{v} - \frac{1 - \theta_w^{v+1}}{v+1} \right]^{\frac{1}{2}} = \frac{\bar{q}}{\sqrt{t}} \quad (1)$$

In this equation, subscript  $e$  signifies conditions in the post-reflected shock region at the edge of the thermal boundary layer and  $w$  signifies conditions at the driven section end wall. Variables  $\rho_e$ ,  $k_{Ae}$ , and  $c_{pe}$  are the density, thermal conductivity, and the specific heat at constant pressure of the gas, respectively.  $T$  is the gas temperature,  $t$  is the time, and  $\theta_w = T_w/T_e$ . Variable  $v$  is a constant set to a value of 0.75, per results from Marineau and Hornung [3] and Fay and Kemp [5].

Based on our target application, our team chose the maximum required heat flux for sensor calibration to be 100 W/cm<sup>2</sup>. One dimensional shock tube analysis was conducted to derive conditions that would meet the maximum required heat flux in a simple shock tube using the relationship described in Eqn. 1. The analysis was completed with the L1d3 code from the University of Queensland [6] a quasi-one dimensional simulation code designed to simulate shock and expansion tube facilities. The proposed shock tube solution utilizes helium and argon as driver and driven gases, respectively. The He-Ar shock tube results in speed of sound ratios sufficient to drive strong shocks, resulting in high post-reflected shock temperatures. Because argon is a monatomic gas, the experimental test conditions are suited to best match the results of perfect gas analysis [4]. Heat flux values in the test region were found by evaluating Eqn. 1 with post-reflected shock temperature and density simulation data. To simplify the analysis, thermal conductivity and specific heat were assumed constant at 1.667 W/(m-K) and 520 J/(kg-K), respectively. These values correspond to the values of argon at 20 C and 1 atm which are the conditions for region 1 (driven section) in the simulated shock tube. Once the required initial pressures were identified, a two dimensional transient analysis was conducted to qualitatively estimate the effects of driver gas contamination, a known cause of early test-time termination in shock tubes [7]. The two dimensional simulation was conducted with Eilmer4, a two- and three-dimensional CFD code developed by the University of Queensland [8.9]. The results of the two simulations were compared to assess the validity of the solutions. The following sections will describe the setup of the one- and two-dimensional simulations as well as the results captured from those simulations.

**1-D Simulation & Design Parameters:** The L1d3 simulation parameters are shown in Table 2. A goal seek analysis was utilized to calculate a  $p_4/p_1$  ratio of 86.5 for tailored shock tube conditions. As test time is dictated by facility size, the design geometry of the shock tube was derived using a Mirel's effect analysis as well as multiple iterations of L1d3 simulations.

**Table 2: 1D Simulation Parameters**

Parameter	Value
<i>Shock Tube Conditions</i>	
Driver Gas	He
Driver Pressure, $p_4$	86.5 atm
Driver Temperature, $T_4$	300 K
Driven Gas	Ar
Driven Pressure, $p_1$	1 atm
Driven Temperature, $T_1$	300 K
<i>Simulation Parameters</i>	
Boundary Conditions	Inviscid, Adiabatic
Gas Model (Driver and Driven)	Ideal

The Mirel's effect describes decreases in ideal shock-contact surface separation caused by boundary layer effects in a shock tube [10]. As shock-contact surface separation increases, the distance between the standing interface and

end wall will increase (see Fig. 7). Maintaining adequate separation is of principle interest, as driver gas contamination at the interface can lead to premature test termination at the end wall [7]. The Mirel's effect analysis concluded that a tube with inner diameter  $d=3$  in and driven length  $l_{DN}=24$  ft resulted in 50% of maximum ideal shock-contact surface separation, corresponding to an interface to end wall separation of 2.89 ft. Preliminary shock tube sizing was deemed acceptable as the  $l_{DN}$  was practical for the planned facility footprint, and interface to end wall separation proved effective for avoiding driver gas contamination within the test time. Analysis of driver gas contamination effects are described in the 2-D simulation results below. L1d3 simulations were completed for shock tube with an  $l_{DN} = 24$ ft, and driver lengths ( $l_{DR}$ ) varying from 3ft to 21ft. A linear test time relationship was derived for increasing driver lengths, shown below in Fig. 8. A driver length of  $l_{DR} = 12$ ft was chosen as the design driver length as it provided adequate test time of 5ms and fit within the planned facility footprint.

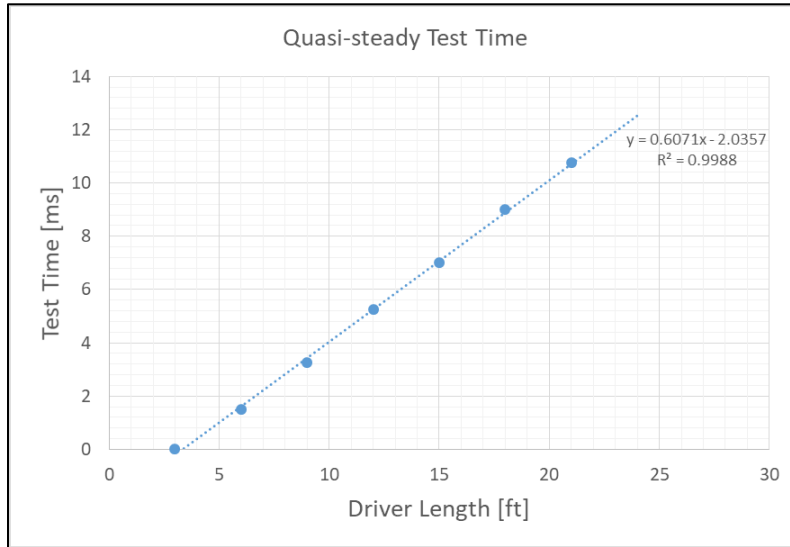


Fig. 8 Test Time vs. Driver Length Relationship

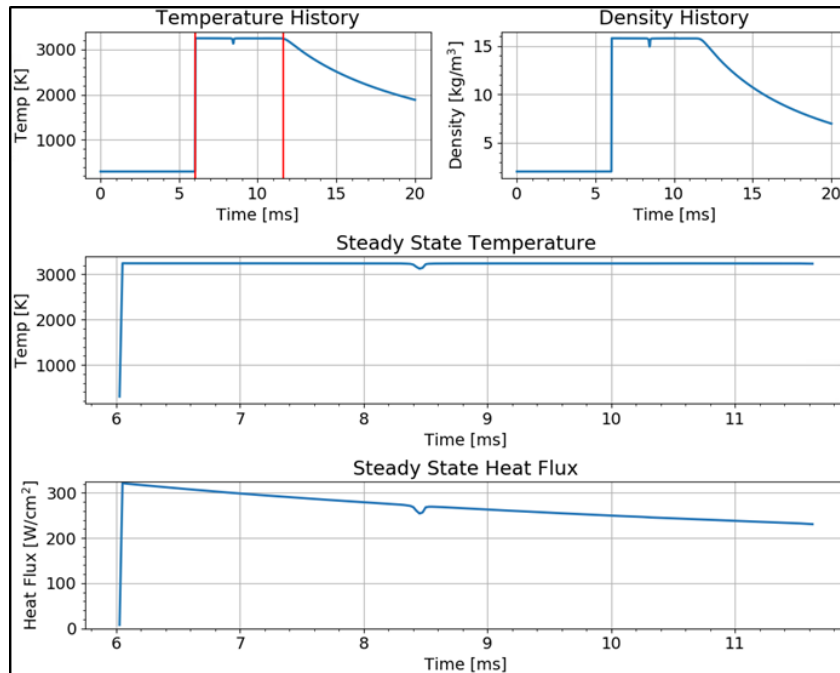
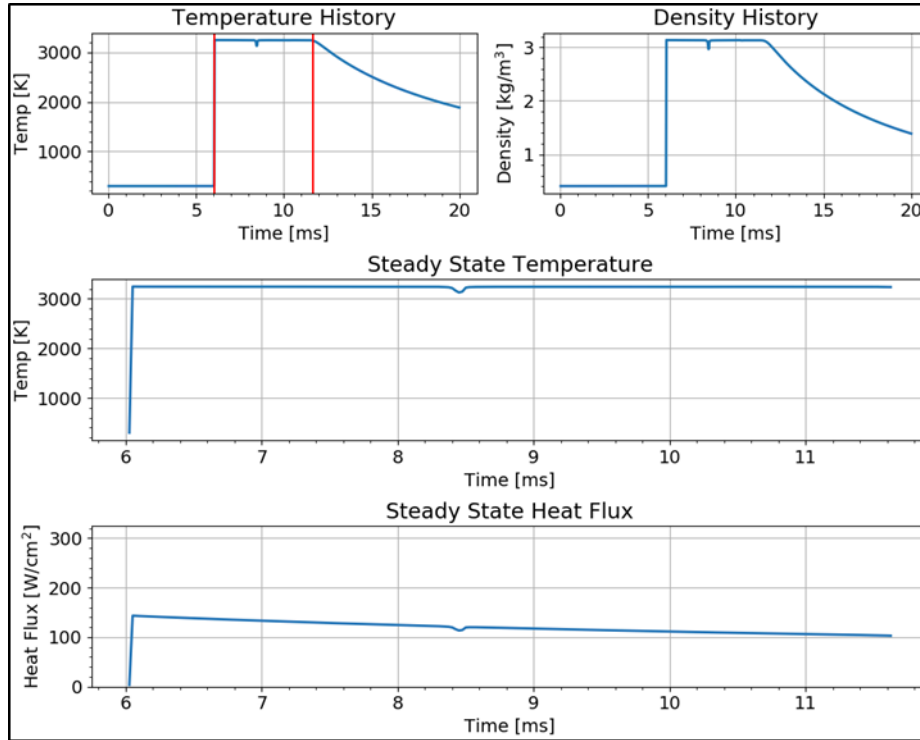


Fig. 9 Heat Flux Conditions for  $p_1 = 1$  atm. Red bars in the temperature history indicate test time.

The L1d3 simulation yielded a quasi-steady test gas temperature of 3244 K and density of 13.2 kg/m<sup>3</sup>, and resulted in steady state heat flux values ranging from 280 to 200 W/cm<sup>2</sup>, exceeding the heat flux values for calibration. These results are shown in Fig. 9. Based on the relationship detailed in Eqn. 1, the heat flux can be decreased by decreasing density via pressure control. By decreasing the driver and driven pressures by a factor of 0.25, the resulting heat flux range is 140 to 100 W/cm<sup>2</sup> (see Fig. 10). This trend is expected as heat flux decreases with the square of density. By adjusting the driven pressure further, various desired heat flux conditions can be generated in the test region. The simulation yielded a quasi-steady test time of 5.5 ms, 5% over the linear model result of 5.25 ms.



**Fig. 10 Heat Flux Conditions for  $p_1 = 0.25$  atm. Red bars in the temperature history indicate test time.**

**Confirmation of Test Conditions with 2-D Simulation:** Following one dimensional analysis, a 2-D viscous simulation was completed using the Eilmer4 code to determine if driver gas contamination terminated the quasi-steady test conditions prior to expansion wave arrival. The simulation boundary conditions utilized adiabatic walls with a no-slip condition, and a laminar viscous model [8-9]. Eilmer4 simulation parameters are shown in Table 3.

**Table 3: 2D Simulation Parameters**

Parameter	Value
<i>Shock Tube Conditions</i>	
Driver Gas	He
Driver Pressure, $p_4$	86.5 atm
Driver Temperature, $T_4$	300 K
Driven Gas	Ar
Driven Pressure, $p_1$	1 atm
Driven Temperature, $T_1$	300 K
<i>Simulation Parameters</i>	
Boundary Conditions	No Slip, Adiabatic
Gas Model (Driver and Driven)	Ideal
Viscous Model	Laminar

The Eilmer4 simulation yielded a quasi-steady test gas temperature of 3130 K (Fig. 11), density of 12.8 kg/m<sup>3</sup>, and test time of 6.2 ms. Test time increased by 12% over the inviscid 1-D simulation, with 3.5% and 3% losses in temperature and density, respectively. These variations can be explained by wave attenuation accounted for by the laminar viscosity model, and result in a 6.4% loss in theoretical heat flux.

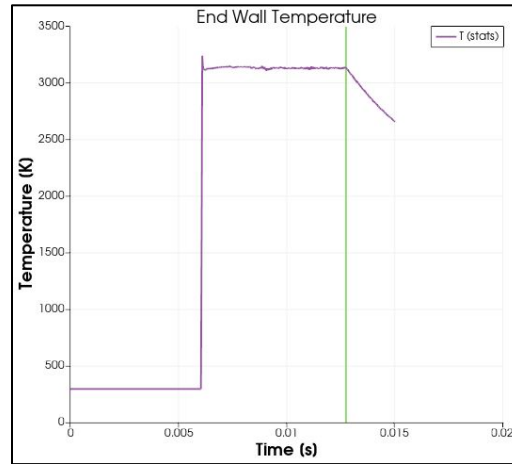


Fig. 11 2-D Simulation temperature-time data

It should be noted that other techniques to test the response time of a heat flux sensor, besides a shock tube/tunnel, includes a laser pulsed facility and an existing reflected shock tunnel. Such facilities exist, as part of Prof. Laurence's laboratory in the Aerospace Engineering Department at the University of Maryland.

### VIII. CFD/Thermal-Structural Analysis Results and Discussion

It's always best, though sometimes not possible, to obtain full CFD/thermal-structural analysis of the flowfield around the heat flux sensor and also within it in order to address some of the challenges and lessons learned described earlier. In order to better understand the thermal-fluid environment around the sensor, with focus on the presence of hot spots and the heat flux distribution, a Computational Fluid Dynamics (CFD) analysis was performed using the commercial CFD code ANSYS Fluent [12-13]. Fluent is a widely used finite-volume code that solves the Reynolds-Averaged Navier-Stokes (RANS) equations. The Fluent solver offers the option to solve the RANS equations using either a pressure-based implicit solver (PBNS) [14-15] or a density-based implicit or explicit solver (DBNS) [16-17] either in steady-state or unsteady mode. ANSYS Fluent is capable of handling both structured and unstructured (Tetrahedral, Cutcell, Polyhedral, Poly-Hexcore, etc.) mesh topologies and it has been extensively validated for high-speed compressible flows [18-19]. In the present work, the numerical results are obtained using the steady-state PBNS in combination with the SST k- $\omega$  turbulence model. The conjugate heat-transfer problem is fully resolved by solving the energy equation for both the fluid domain and the solid flat plate/sensor assembly in a coupled manner. All results are fully converged to a steady-state solution and are second-order (upwind) accurate for the convective fluxes and second-order (central) accurate for the diffusive fluxes.

Prior to implementing a heat flux sensor and installing it within a test article ("parent" material) in a high enthalpy, high Mach # aero-propulsion wind tunnel or on a flight vehicle, its best to perform either a 1D heat transfer analysis or a full 2D or 3D thermal-fluid/thermal-structural analysis on the sensor/test article combination to help predict the thermal response of each component to the flow field. Such analysis will help mitigate some of the challenges outlined earlier as well as provide some confidence in how the sensor will respond/perform in its final application. In this section, a 3D CFD/FEA analysis is presented, serving as a case study for implementing the heat flux sensor in Fig. 14 into a Mach 2 flow in the iCAT (Innovating Continuous Air Tunnel) facility in Ronkonkoma, NY. Objectives for this type of analysis were to: (1) model the heat flux sensor and its sub-components, as installed into its test plate, within the iCAT facility; (2) assess the heat flux sensor's thermal response to the expected thermal-fluid environment; (3) study the sensor's thermal response for different sensor packaging materials as well as different materials of the test article, per Table 5; (4) determine if hot spots and 2D heat transfer effects exist between the sensor and its test plate due to dissimilar material's thermal conductivity and  $(\rho C_p k)^{1/2}$  factors; (5) perform material parametrics to

determine which combination of test article (“parent”) and sensor materials displayed minimal hot spots with minimal 2D heat transfer effects.

In the specific case study presented here, the heat flux sensor head is a Si MEMS die, Sensor Part 2, Fig. 14, with two gold contact pads, Sensor Parts 1,3 Fig. 14, was simulated along with several Type K thermocouples installed into the sensor body and its packaging, Fig. 14. Installation of these thermocouples enables determine whether hot spots and 2D heat transfer effects exist within the sensor/parent material combination, during Mach 2 testing. The domain shape and nominal size are shown in Fig. 12. Note that no attempt was made to simulate the nozzle shape at the top of the wind tunnel. Only half of the domain was simulated since the geometry and the flowfield are symmetric about the tunnel centerline. Only the location of 2 thermocouples to the side of the sensor is not symmetric, but the influence of this asymmetry is negligible. No slip wall was applied at the surface of the solid test article/plate and of the sensor while slip wall boundary conditions together with adiabatic assumption was applied to the sides and to the top of the wind tunnel.

The inlet was modeled using the nominal Mach number of 2.0 and an inlet boundary layer 3mm thick was assumed to follow the 1/7<sup>th</sup> power law and applied at the upstream boundary using Fluent built-in expressions. Outlet conditions were set as constant pressure. The flat plate/wind tunnel floor was assumed to be of uniform 0.5inch in thickness and made of SS 304 stainless steel. A convection heat transfer boundary condition was applied on the far side of the solid wall, with a room temperature assumed to be at 293K and an h of 2.0 W/m<sup>2</sup>-K. All of the conditions used in the simulation are summarized in Table 4 while Fig. 13 shows the shape of the computational domain on the left, and the mesh on the symmetry and inlet boundaries, with a detailed view of the region around the heat flux sensor. The geometric model of the sensor used in the CFD analysis is show in Fig. 14 which shows the different components of the sensor (the 6 thermocouples, 2 of which are embedded in the material, the 3 sensor parts, the sensor base) and the material they are made of. Some parts of the sensor structure were simplified to facilitate the analysis, for example, the actual central sensor part (Part 2 in Fig. 14,) is made of solid silicon.

The computational mesh was generated using FLUENT Meshing. The mesh is a combination of prisms in the inflation layers and polyhedral cells in the freestream and in the solid zones. An initial mesh with 4.6M cells was used to obtain an initial solution and was refined using Fluent mesh adaption to a mesh size of 56.5M cells, with a maximum aspect ratio of 3000 and an orthogonal quality of 0.10 as defined in the FLUENT User’s Guide [12].

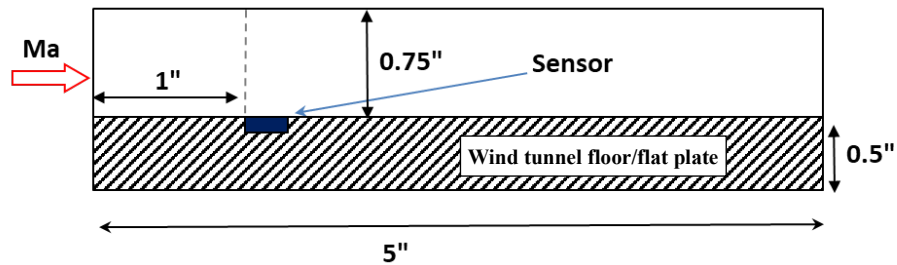
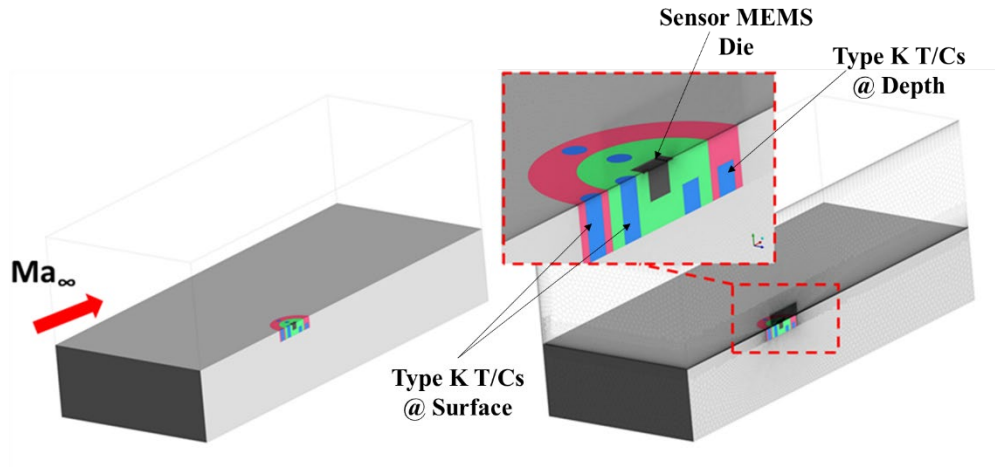


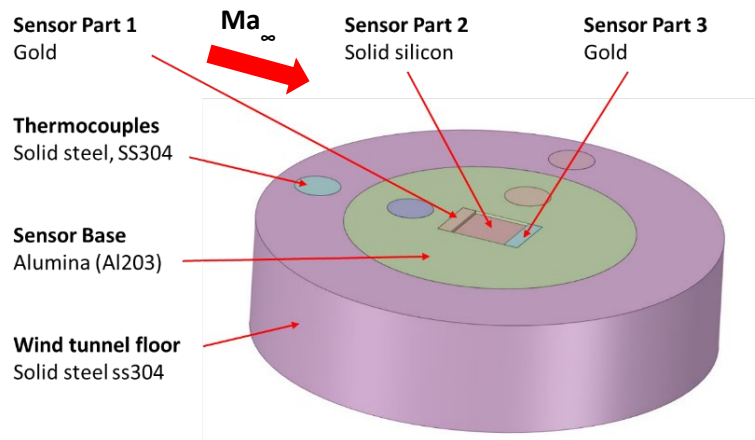
Fig. 12 Domain size with heat flux mounted in the flat plate.

Table 4 Boundary conditions for the wind tunnel CFD simulation.

Parameter	Value
Gas	Air, perfect gas ( $\gamma=1.40$ )
$M_\infty$	2.0
$P_{\infty, t}$	3,511.7e+03 Pa
$P_\infty$	44,881 Pa
$T_\infty$	265.3 K
$T_{\infty, t}$	477.5 K
Type of boundary layer	Turbulent (SST $k-\omega$ ) TI =5%, $\mu_T/\mu=1.0$
Inlet boundary layer ( $\delta_0$ )	3 mm
Velocity profile	$\frac{U}{U_c} = \left(\frac{y}{\delta}\right)^{\frac{1}{7}}$



**Fig. 13** iCAT facility wind tunnel domain and mesh, with details of the heat flux sensor.



**Fig. 14** Heat flux sensor materials. Sensor base diameter is 5 mm, thickness is 2mm.

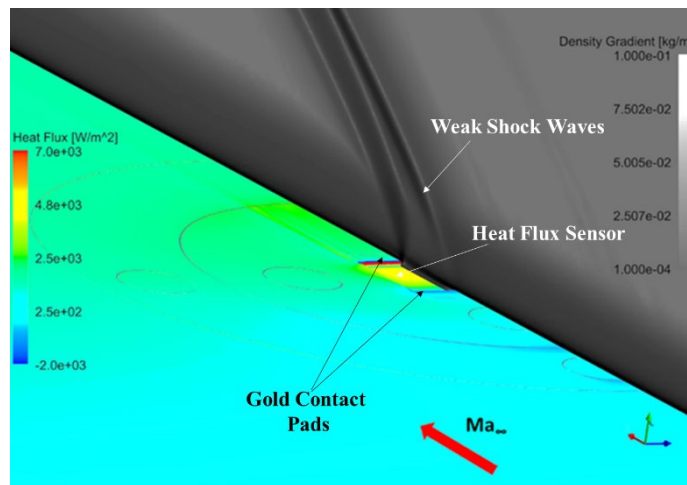


**Fig. 15** Heat flux contours on sensor with test article, with simulated Schlieren on symmetry plane.

Figure 15 shows the results of the CFD simulation, with the computed heat flux mapped on the solid top surface of the sensor and of the flat plate, and the simulated Schlieren photograph on the midplane. The complexity of the flowfield around the sensor is put in evidence by the shock formations created by the sensor shallow surface recess. It is also noticeable the increase in heat flux on the sensor forward-facing vertical surface. Notice also how a vortex is forming at the downstream corner of the sensor, shown by the decrease of the local heat flux along its downstream trajectory. Figs. 15-16 show a side view of the simulated Schlieren photograph and of the temperature distribution through the plate thickness, both plotted on the tunnel midplane.

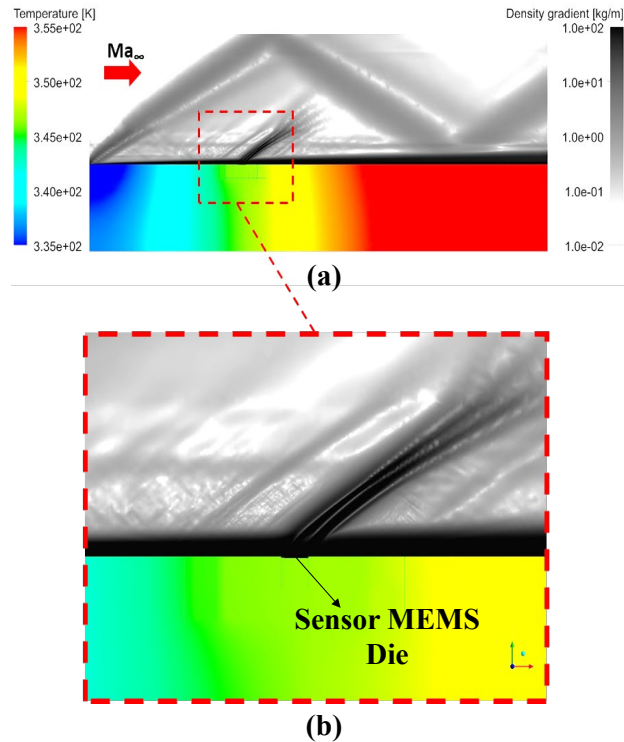


**Fig. 16 Side view of temperature distribution through the flat plate thickness and Schlieren picture on the plane of symmetry of the tunnel: (a) entire domain and (b) heat flux sensor.**

From Fig. 16a, it is clear that the major temperature gradients through the flat plate thickness are two-dimensional, with a linear streamwise increase in the temperature. The flowfield is characterized by a growing turbulent boundary layer. There is a weak boundary-layer-induced shock at the inlet of the domain, which reflects off the top and bottom walls of the wind tunnel; this weak shock is a result of the estimated inlet boundary layer profile interacting with the supersonic inlet. Also, the multiple shock formation created by the sensor recess is clearly visible in the detail view, Fig. 16b. These shocks are weak and do not create any appreciable change in the boundary layer or the thermodynamic state around the sensor. For hypersonic conditions,  $> \text{Mach } 5$ , such CFD would help determine how the heat flux sensor's installation affects its performance and the flowfield surrounding it.

While no canonical validation of CFD results against experimental data has been performed in the present work, the numerical results still represent a useful tool for qualitatively understanding the flowfield created by heat flux sensors and to guide the design of such sensors. Such a validation of the numerical analysis will be performed in future work, together with the fine-tuning of the boundary conditions for the wind tunnel flow. To accomplish such a goal, a thorough characterization of the wind tunnel flow will be performed so as to better understanding any flow variability. Once the CFD approach is validated, a thorough parametric study will be carried out under different flow conditions to explore and better understand the operating envelope of the sensor.

In order to characterize the temperature distribution within the heat flux sensor head and the sensitivity of that distribution to the test article materials and to the materials used to construct the sensor, as well as to assess hot spot/2D

heat transfer affects, steady-state Finite Element Analysis (FEA) simulations of heat conduction through the sensor were conducted using ANSYS Mechanical, [19]. ANSYS Mechanical is an ANSYS Workbench application that can perform a variety of engineering simulations, including stress, thermal, vibration, thermo-electric, and magneto-static simulations. ANSYS Mechanical is capable of handling both structured and unstructured mesh topologies and has a number of options for boundary conditions and contacts between elements to support different loading and support cases.

The domain shape is documented in Fig. 17. The computational domain includes a ceramic sensor head containing a silicon chip and two gold electrical leads, embedded in a 1-inch cube of stainless steel parent material. The computational domain also includes six thermocouples, four of which penetrate the entire thickness of the parent material, two of which stop at a depth of 0.001 m from the face in which the sensor head is embedded. These thermocouples are 0.03125" wide and are composed of a 0.005"-thick sheath of Stainless Steel 304 (SS304) around a core of Magnesium Oxide (MgO). Material properties for all materials simulated were gathered from a variety of sources [20-32]. The generated volume mesh contains 106,264 cells with edge lengths from 1e-7 m to 1e-3 m.

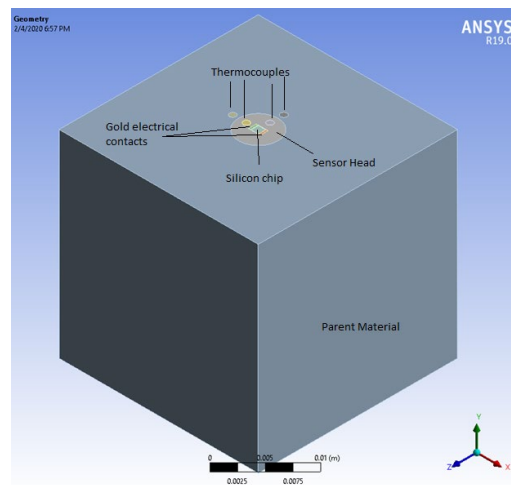


**Fig. 17** Computational domain geometry for heat flux sensor/test article combination

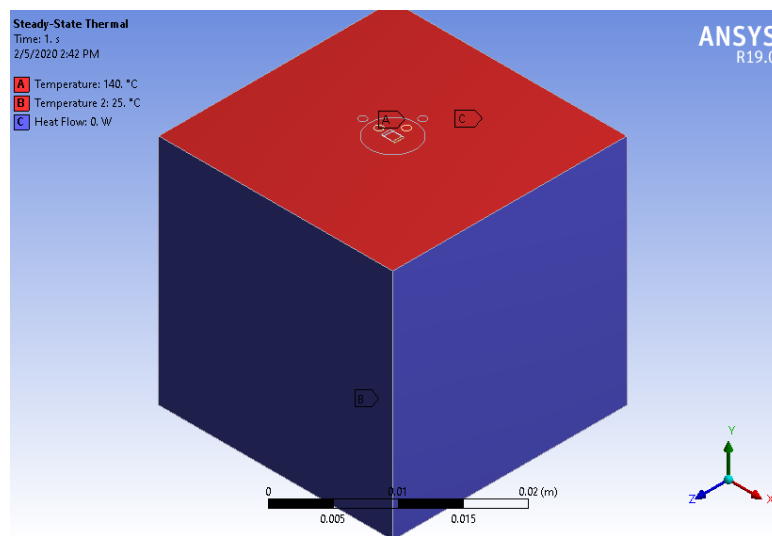


**Fig. 18** Boundary Conditions on Static Thermal Simulation

In total, seven steady-state simulations were executed in this effort, as tabulated in Table 5. Six of these simulations were steady-state thermal simulations which applied a constant 140°C boundary condition to one face of the computational domain, representing the face exposed to the hot air flow in iCAT, a constant 25°C boundary condition to the opposite face (representing the room-temperature side), and perfect insulation on the other four faces (representing the walls embedded in more parent material), as shown in Fig. 18. These conditions are representative of Mach 2 flow in the Innovating iCAT facility. These simulations also varied the composition of the parent material and the sensor head. The parent material was either SS304 or another stainless steel alloy, 15-5PH (SS15-5PH). The sensor head material was either alumina (Al<sub>2</sub>O<sub>3</sub>), machinable ceramic (MaCOR), or zirconia (ZrO<sub>2</sub>). All possible combinations of these materials were simulated with the same boundary conditions to compare the internal temperature distribution in each case and to assess and mitigate possible hot spots, 2D heat transfer.

**Table 5: Simulations Conducted**

Simulation	1	2	3	4	5	6	7
Type	Steady Thermal	Steady Structural					
Parent Material	SS 304	SS 304	SS 304	SS 15-5PH	SS 15-5PH	SS 15-5PH	SS 304
Sensor Material	Al <sub>2</sub> O <sub>3</sub>	MaCOR	ZrO <sub>2</sub>	Al <sub>2</sub> O <sub>3</sub>	MaCOR	ZrO <sub>2</sub>	Al <sub>2</sub> O <sub>3</sub>
Boundary Conditions	25-140°C on opposing faces, insulated on other faces	25-140°C on opposing faces, insulated on other faces	25-140°C on opposing faces, insulated on other faces	25-140°C on opposing faces, insulated on other faces	25-140°C on opposing faces, insulated on other faces	25-140°C on opposing faces, insulated on other faces	Frictionless supports on three adjacent faces, temperature distribution imported from steady thermal simulation
Ratio of $\sqrt{\rho c_p k}$ of parent/sensor material	0.76	9.01	3.2	0.71	8.42	2.99	0.76

An additional steady-state structural simulation was executed using a combination of S S304 parent (i.e. test article) material and Al<sub>2</sub>O<sub>3</sub> sensor head material. This simulation fed in the temperature distribution from the steady-state thermal simulation with that combination to study the effects of free thermal expansion in the sensor head and parent material. To take into account gap formation as a result of thermal expansion, non-linear “rough” and “frictionless” contacts were applied to some joints between materials in place of the default “bonded” contacts. In an ANSYS Mechanical “bonded” contact, two parts cannot move relative to one another. In a “rough” contact, a gap can form between them but they will not slide against one another. “Rough” contacts are used on faces that will be press-fit in the actual sensor, such as the interface between the sensor head and the parent material, and between the thermocouples and the parent material and the sensor head. In a “frictionless” contact, faces can slide against one another freely and gap formation is possible. These contacts are applied to the interfaces between the electrical components of the sensor, eg. the gold electrical leads and the silicon die.

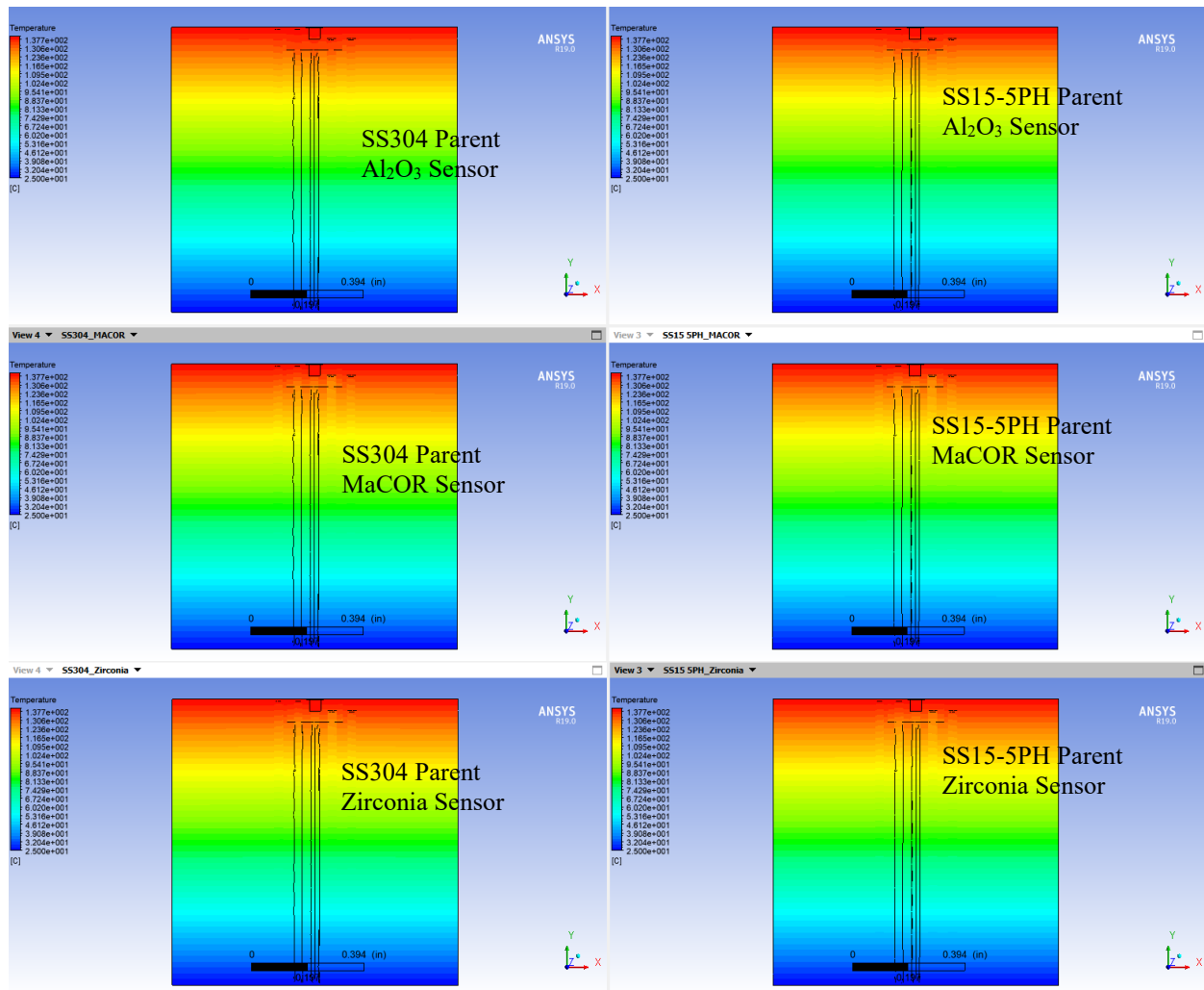


**Fig. 19** Temperature Distribution in Six Static Thermal Simulations from 25°C to 140°C

In the steady-state structural simulation, three faces of the parent material cube receive frictionless support boundary conditions. These supports constrain the body's movement in the directions normal to those faces. These boundary conditions allow the computational domain to expand freely in the three special dimensions. Figure 19 shows the temperature distribution across a section through the center of the parent material cube for each of the six steady-state thermal simulations conducted in this effort. The temperature scale in Fig. 19 is from 25°C to 140°C. In each simulation, the temperature distribution is grossly longitudinal, with a gradient from the heated face to the room-temperature face of the cube. There is no apparent radial temperature gradient, and no readily-apparent difference caused by the different material combinations, indicating no hot spot and no 2D heat transfer affects/issues at these Mach 2 test conditions.

Figure 20 zooms the view in to the sensor head and surrounding thermocouples for each of the six simulations, with a temperature scale revised to 125°C-140°C. At this magnification, there is a greater difference in temperature distribution between the different material combinations. The difference in parent material has no significant effect on its temperature distribution (unsurprising, since both parent materials are stainless steel and have very similar heat capacities and thermal conductivities [21][30][31]). The sensor head material has a more pronounced impact on temperature distribution. The simulations conducted with an  $\text{Al}_2\text{O}_3$  sensor head show greater penetration of heat into the sensor, with a temperature of 136°C at the bottom of the silicon component, compared to 134°C with the other two sensor materials. The thermocouples in the sensor head are also much warmer in the simulation with the  $\text{Al}_2\text{O}_3$  sensor than the other simulations and show deeper thermal penetration. This is consistent with  $\text{Al}_2\text{O}_3$  having a thermal

conductivity an order of magnitude higher than either of the other two ceramics [22], [25], [32]. The greater thermal conductivity of  $\text{Al}_2\text{O}_3$  also leads to the silicon sensor chip being cooler in simulations with an  $\text{Al}_2\text{O}_3$  sensor head, because the  $\text{Al}_2\text{O}_3$  more efficiently conducts heat away from the chip.

For Fig. 20 magnification, the temperature gradient in the sensor at a steady-state is still primarily longitudinal in all simulations. A very small radial temperature gradient ( $1^\circ\text{C}$  from one side of the thermocouple to another) can be observed in the simulations with  $\text{ZrO}_2$  and MaCOR sensor heads. Neither Fig. 19 nor Fig. 20 show any sign of hot spots or 2D heat transfer effects within and around the sensor, at steady-state operation.

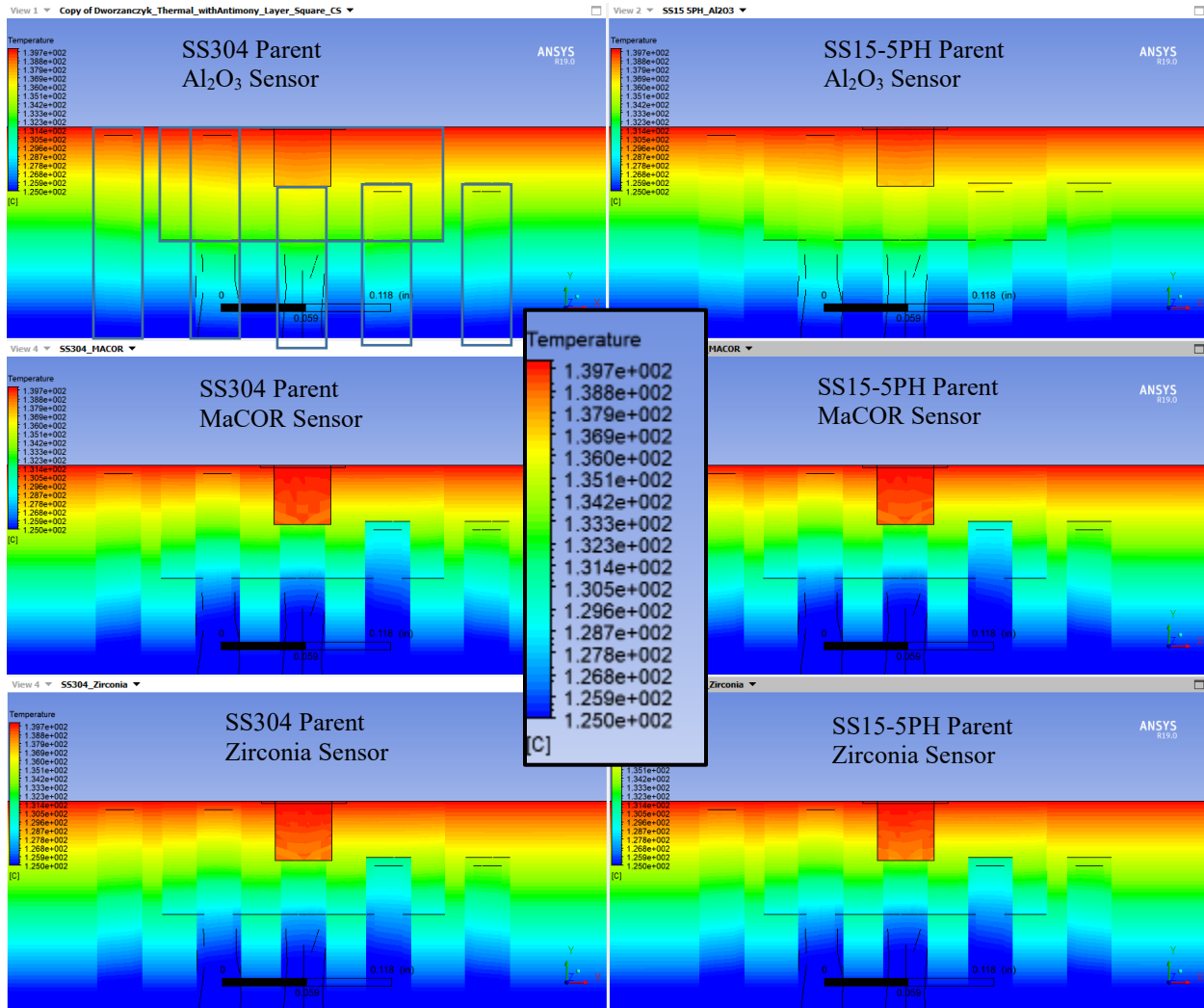


**Fig. 20 Temperature Distribution in Six Static Thermal Simulations, Sensor Head Magnified**

Figure 21a shows the maximum principle stresses on the entire computational domain for the SS304/ $\text{Al}_2\text{O}_3$  simulation. A maximum principle stress of 65.698 MPa (compressive) and a minimum of 16.858 MPa (tensile) are calculated, but neither is visible in Fig. 21b. Instead, very low-magnitude stresses are present on the parent material and slightly greater ( $<10$  MPa compressive) stresses are visible on the sensor head. Figure 21b shows the maximum principle stresses on the sensor head alone. The minimum principle stress (or greatest tensile stress) is shown to be around the circumference of the  $\text{Al}_2\text{O}_3$  sensor head. The maximum principle stress (also greatest compressive stress) is on the faces where the gold electrical contacts meet the sensor head. The tensile stresses are approximately a factor of 20 less than the yield stress of  $\text{Al}_2\text{O}_3$ , and do not pose a threat of damaging the sensor. Tensile stresses along the circumference may result from the steel thermocouples, whose coefficient of thermal expansion expands that of  $\text{Al}_2\text{O}_3$  but which are press-fit in place, may be stretching the  $\text{Al}_2\text{O}_3$ . The greatest compressive stresses are found where the gold (which also has a higher coefficient of thermal expansion than  $\text{Al}_2\text{O}_3$ ) meets the sensor head. These stresses are

approximately 5 times lower than the yield stress of  $\text{Al}_2\text{O}_3$ , but in practice would actually be lower than the simulation predicts because the gold may expand outward into the free space above the sensor head instead of pressing against the sensor material.

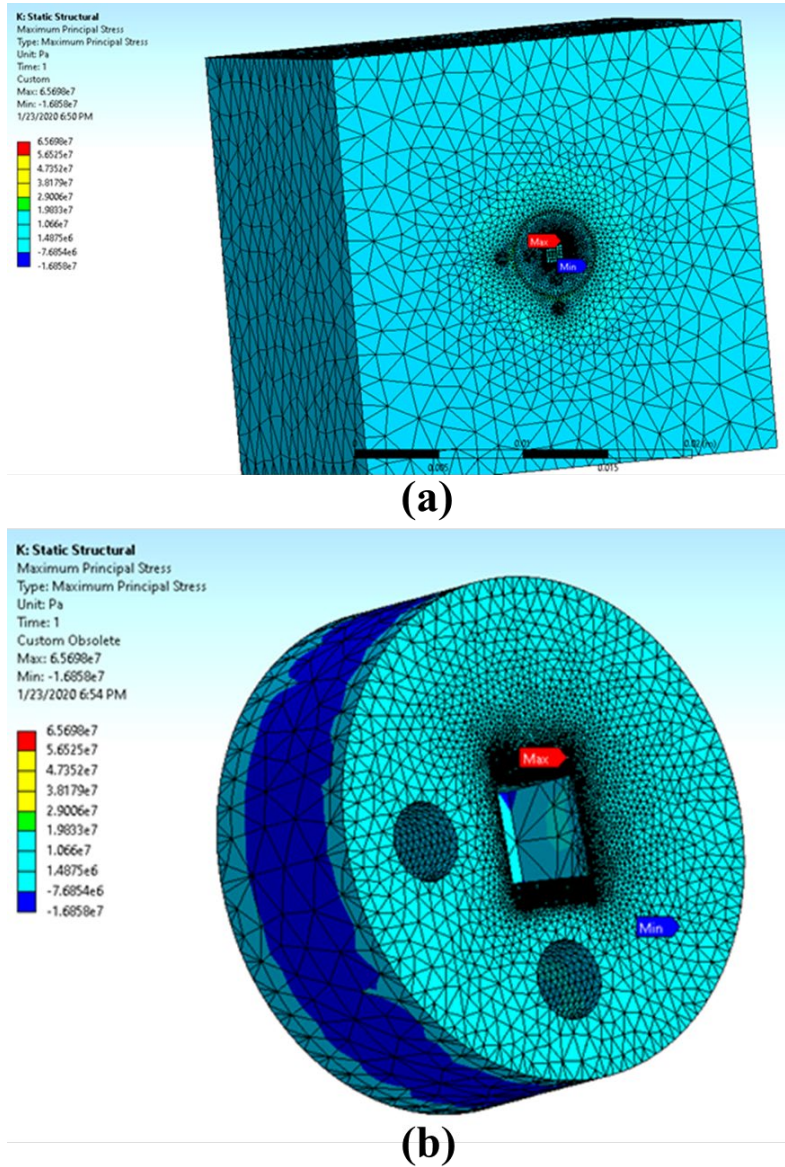


**Fig. 21 (a) Stresses on sensor and parent material; and (b) Stresses on sensor head alone SS 304/ $\text{Al}_2\text{O}_3$  combination**

No compressive stresses are observed on the joints between the sensor head and the parent material because the steel parent material has a higher coefficient of thermal expansion than the sensor head material in all cases, so a gap is always expected to form at that interface. This analysis has found that, in steady-state operation in the iCAT wind tunnel, none of the proposed combinations of parent material and sensor head material will result in hot spots in the sensor. All combinations will have a mostly-longitudinal temperature gradient. The stresses on the sensor and parent material with an SS304/  $\text{Al}_2\text{O}_3$  combination are under the yield stresses of  $\text{Al}_2\text{O}_3$  with a factor of safety of at least 5.

This analysis, simulating the steady-state temperature distribution in the sensor and parent material, is not applicable to sensor behavior in the Arnold Engineering Development Center (AEDC) Tunnel 9 facility, because that facility operates in a transient mode with short run times (0.25 s to 5 s) [16]. This may not be enough time for the sensor and parent material to reach equilibrium with their surroundings and therefore a steady state. In these short time spans,

the heat capacity of the materials in the simulation can have a significant impact on the temperature distribution. As such, a further analysis must simulate transient heating of the sensor and parent material in order to understand the temperature distribution at different times during a wind tunnel test.

The next step, therefore, must be to acquire heat transfer data from either experimental measurements of the iCAT and AEDC Tunnel 9 wind tunnels or computational simulations thereof, and to apply this heat transfer data to transient, time-varying simulations of the sensor. Temperature distributions at different times in the simulation can then be used to calculate thermal expansion loads in the unevenly-heated sensor.

## IX. Conclusion

Implementing heat flux sensors for hypersonic applications presents a unique set of challenges requiring careful balance of analysis, design and calibration to obtain accurate and useful experimental data. This work presented an overview of some calibration techniques for heat flux sensors, with a focus on shock tube analysis, design. 3D steady state CFD ANSYS FLUENT analysis provides a useful tool for qualitatively understanding the flowfield created by heat flux sensors and to guide the design of such sensors. To characterize the temperature distribution within the heat flux sensor head and the sensitivity of that distribution to the test article materials and to the materials used to construct the sensor, as well as to assess hot spot/2D heat transfer affects, a steady-state 3D thermal-structural analysis using ANSYS Mechanical was developed. Preliminary parametrics were conducted and included varying the test article material from SS-304 to SS 15-5PH and changing the heat flux sensor packaging material from  $\text{Al}_2\text{O}_3$ , to MaCOR to  $\text{ZrO}_2$ . This analysis showed that for steady-state operation in the Innoveering iCAT Mach 2 wind tunnel, none of the proposed combinations of parent (test article) and sensor head materials result in hot spots in the sensor. All combinations showed a relatively dominate longitudinal temperature gradient and therefore no 2D heat transfer effects, allowing for simple interpretation of the heat flux data from the sensor. The stresses on the sensor and parent material with an SS304/  $\text{Al}_2\text{O}_3$  combination are under the yield stresses of  $\text{Al}_2\text{O}_3$  with a factor of safety of at least 5. These results are typical of the kind of analysis that is very useful in designing and implementing heat flux sensors for hypersonic applications.

## Acknowledgments

The authors would like to acknowledge the assistance provided by the following: ANSYS, Inc; Dr. Robert Bakos (Principal, Innoveering), Dr. Dean Modroukas (Principal, Innoveering), Grace Correa (Innoveering), Frank Celentano (Innoveering); Jiaji Li (Innoveering), Christian Petrov (Innoveering), and Alex Dworzanczyk (Innoveering) for providing valuable contributions/discussions with regards to shock tube design/analysis, heat flux sensor renderings, and thermal-structural FEA (ANSYS) results conducted for this work.

## References

- [1] Smith, V.K., Matthews, R.K., and Maus, J.R., Hypersonic Flight Testing, AEDC Technical Report AEDC TR-94-7, August 1994.
- [2] Boutier, A., "New Trends in Instrumentation for Hypersonic Research", NATO ASI Series E: Applied Sciences, Vol 224. Article is: "Temperature and Heat Flux Measurements-Challenges for High Temperature Aerospace Application", written by Richard D. Neumann, University of Dayton Research Institute, pp 409-435.
- [3] Murthy, A.V., Tsai, B.K., and Saunders, R.D., "Radiative Calibration of Heat Flux Sensors at NIST: Facilities and Techniques", J. Res. Natl. Inst. Stand. Technol. **105**, 293 (2000).
- [4] Marineau, E. C., and Hornung, H. G., "Modeling and Calibration of Fast-Response Coaxial Heat Flux Gages," *47<sup>th</sup> AIAA Aerospace Sciences Meeting*, AIAA, Orlando, FL, 2009. <https://doi.org/10.2514/6.2009-737>
- [5] Anderson, John D. Chapter 7, *Modern Compressible Flow: With Historical Perspective*. Boston: McGraw-Hill, 2003. Print.
- [6] Fay, J. and Kemp, N., "Theory of Heat Transfer to a shock-tube end-wall from an ionized monoatomic gas," *The Journal of Fluid Mechanics*, Vol. 21, 1965, pp. 659-672.
- [7] Jacobs, P. A., "Shock Tube Modeling with L1d." University of Queensland, Department of Mechanical Engineering, 1998.
- [8] Stalker, R. J., and Crane, K. C. A., "Driver Gas Contamination in a High-Enthalpy Reflected Shock Tunnel," *AIAA Journal*, vol. 16, pp. 276-279.
- [9] Jacobs, P. A., and Gollan, R. J., "Implementation of a Compressible-Flow Simulation Code in the D Programming Language," *Advances of Computational Mechanics in Australia*, vol. 846, pp. 54-60. <https://doi.org/10.4028/www.scientific.net/AMM.846.54>
- [10] Gollan, R. J., and Jacobs, P. A., "About the formulation, verification and validation of the hypersonic flow solver Eilmer," *International Journal for Numerical Methods in Fluids*, vol. 73, pp. 19-57. <https://doi.org/10.1002/flf.3790>
- [11] Mirels, H., "Shock Tube Test Time Limitation Due to Turbulent-Wall Boundary Layer," *AIAA Journal*, vol. 2, pp. 84-93.

- [12] ANSYS, Inc., ANSYS Fluent User's Guide, Release 2019R3, 2019.
- [13] ANSYS, Inc., ANSYS Fluent Theory, Release 2019R3, 2019.
- [14] Kim, S.E., Mathur, S., Murthy, J., Choudhury, D., A Reynolds-averaged Navier-Stokes solver using unstructured mesh-based finite-volume scheme, 36th AIAA Aerospace Sciences Meeting and Exhibit, 1998.
- [15] Kim, S.E., Makarov, B., An implicit fractional-step method for efficient transient simulation of incompressible flows, 17th AIAA Computational Fluid Dynamics Conference, 2005.
- [16] Weiss, J. W., Maruszewski, J. P., Smith, W. A., Implicit Solution of Preconditioned Navier-Stokes Equations Using Algebraic Multigrid, AIAA Journal, Volume 37, Number 1, January 1999.
- [17] Weiss, J. W., Smith, W. A., Preconditioning Applied to Variable and Constant Density Flows, AIAA Journal, Volume 33, Number 11, January 1995.
- [18] Rao, V., Viti, V., Abanto, J., "CFD simulations of super/hypersonic missiles: validation, sensitivity analysis and improved design", accepted for publication at AIAA ScitTech 2020, Orlando, FL, January 6-10th, 2019.
- [19] Kurbatskii, K.A., Kumar, R., and Mann, D., "Simulation of External Hypersonic Problems Using Fluent 6.3 Density-Based Coupled Solver", 2<sup>nd</sup> European Conference for Aerospace Sciences
- [20] ANSYS, Inc., ANSYS Mechanical User's Guide, Release 15.0, November 2013
- [21] "304 SS," MATWEB, <http://www.matweb.com/search/DataSheet.aspx?MatGUID=abc4415b0f8b490387e3c922237098da>, accessed 1/16/2020
- [22] "Corundum, Aluminum Oxide, Alumina, 99.9%, Al<sub>2</sub>O<sub>3</sub>," MATWEB, [www.matweb.com/search/DataSheet.aspx?MatGUID=c8c56ad547ae4cfabad15977bfb537f1](http://www.matweb.com/search/DataSheet.aspx?MatGUID=c8c56ad547ae4cfabad15977bfb537f1).
- [23] "Silicon, Si," MATWEB, [www.matweb.com/search/DataSheet.aspx?MatGUID=7d1b56e9e0c54ac5bb9cd433a0991e27](http://www.matweb.com/search/DataSheet.aspx?MatGUID=7d1b56e9e0c54ac5bb9cd433a0991e27).
- [24] "High Temperature Ceramics," Cotronics, <http://www.cotronics.com/catalog/56%20%20%20915%20%2056L.pdf>.
- [25] "MACOR: Machinable Glass Ceramic for Industrial Applications," Corning, <http://www.cotronics.com/catalog/56%20%20%20915%20%2056L.pdf>
- [26] "Gold, Au," MATWEB, [www.matweb.com/search/DataSheet.aspx?MatGUID=d2a2119a08904a0fa706e9408cddb88e](http://www.matweb.com/search/DataSheet.aspx?MatGUID=d2a2119a08904a0fa706e9408cddb88e)
- [27] "Properties: Magnesia – Magnesium Oxide (MgO) Properties & Applications," AZO Materials, <https://www.azom.com/properties.aspx?ArticleID=54>.
- [28] Peterson, Kurt E. "Silicon as a Mechanical Material," Proceedings of the IEEE, Vol 70, No 5, May 1982. <http://inst.cs.berkeley.edu/~n245/fa01/PETERSEN.PDF>.
- [29] "Material: Aluminum Oxide (Al<sub>2</sub>O<sub>3</sub>), bulk." MEMSNet, <https://www.memsnet.org/material/aluminumoxideal2o3bulk/>, accessed 1/17/2020, citing "CRC Materials Science and Engineering Handbook, p. 473"
- [30] "AK Steel 15-5 PH® Precipitation Hardening Stainless Steel, Condition H 900," MATWEB, <http://www.matweb.com/search/datasheet.aspx?MatGUID=54cf2c4d5b4b411ca142008eb02d7a62>,
- [31] "AK Steel 15-5 PH® Stainless Steel," AK Steel, 03/31/2017, <https://www.aksteel.com/sites/default/files/2018-01/155ph201706.pdf>.
- [32] "CeramTec 848 Zirconia (ZrO<sub>2</sub>)," MATWEB, <http://www.matweb.com/search/DataSheet.aspx?MatGUID=05e29689151440d3904052baa788ae22>
- [33] Ultrafast Heat Transfer Sensor: ALTP Users Manual, supplied by ForTech HTS GmbH
- [34] Kegerise, M., and Rufer, S., "Unsteady heat-flux measurements of second-mode instability waves in a hypersonic flat-plate boundary layer", Experiments in Fluids, Vol. 57, 130, 2016.
- [35] Roediger T, Knauss H, Kraemer E, Wagner S, Bountin D, Smorodsky B, Chirkashenko V, Zvegintsev V, and Maslov A, "Atomic layer thermopile - a fast heat-flux sensor for measuring high heat loads in short-duration hypersonic ground testing facilities", in: Proc. ICMAR 2007, Novosibirsk, Russia, Pt. 4, P. 154-166, 2007